Burns & Trauma, 2026, 14, tkag036
https://doi.org/10.1093/burnst/tkag036
Published: 19 May 2026
Research Article

OXFORD

Preclinical evaluation of a bioartificial kidney loaded with functional renal tubular cells in a Bama miniature pig model of acute renal failure

Yunming Xiao[1,2,‡], Chuyue Zhang[2,3,‡], Tianyi Yang[4,‡], Yiyu Huang[1,2], Xu Wang[1,2], Xiaoxiao Liu[5], Mengfei Li[1,2], Shaoyuan Cui[1,2], Guangrui Geng[1,2,6], Xiang Li[4,*], Qinggang Li[1,2,*], Xiangmei Chen[1,2,*]

[1]Postgraduate School, Medical School of Chinese PLA, No. 28 Fuxing Road, Haidian District, Beijing 100853, China
[2]Senior Department of Nephrology, Chinese PLA General Hospital, State Key Laboratory of Kidney Diseases, National Clinical Research Center for Kidney Diseases, Beijing Key Laboratory of Medical Devices and Integrated Traditional Chinese and Western Drug Development for Severe Kidney Diseases, Beijing Key Laboratory of Digital Intelligent TCM for the Prevention and Treatment of Pan-vascular Diseases, Key Disciplines of National Administration of Traditional Chinese Medicine (zyyzdxk-2023310), Innovation Team and Talents Cultivation Program of National Administration of Traditional Chinese Medicine (No: ZYYCXTD-D-202402), No. 28 Fuxing Road, Haidian District, Beijing 100853, China
[3]Department of Nephrology and Institute of Kidney Diseases, West China Hospital, Sichuan University, No. 37 Guoxue Alley, Wuhou District, Chengdu 610041, China
[4]Alan G. MacDiarmid Institute, College of Chemistry, Jilin University, No. 2699 Qianjin Street, Chaoyang District, Changchun 130012, China
[5]Department of Nephrology, The Second Medical Center of Chinese PLA General Hospital, No. 28 Fuxing Road, Haidian District, Beijing 100853, China
[6]Department of Critical Care Medicine, 920th Hospital of Joint Logistics Support Force of Chinese PLA, No. 212 Daguan Road, Xishan District, Kunming 650032, China

*Corresponding authors. Xiangmei Chen, E-mail: xmchen301@126.com; Qinggang Li, E-mail: lqgbj301@126.com; Xiang Li, E-mail: xiangli@jlu.edu.cn.
‡Yunming Xiao, Chuyue Zhang and Tianyi Yang contributed equally to this work.

Abstract

Background: **Severe acute kidney injury (AKI) is associated with high mortality. Current blood purification technologies fail to replace the biological functions of renal tubular epithelial cells (RTECs), such as active transport, acid–base homeostasis, and endocrine regulation. The integration of viable RTECs into an extracorporeal circuit to construct a bioartificial kidney represents a potential strategy for renal functional support. However, its translation is constrained by the rapid loss of seed cell phenotypes, immune and coagulation activation triggered by conventional materials, and a lack of *in vivo* validation in large animal models. However, three key challenges hinder its clinical translation, which this study seeks to address: the rapid loss of seed cell phenotypes, immune and coagulation activation triggered by conventional materials, and a lack of *in vivo* validation in large animal models.**

Methods: **We engineered a renal tubule assist device (RAD) that integrates viable cells with a functionalized interface. First, we established an immortalized human proximal tubule cell line [immortalized renal tubular epithelial cell line (iRTEC)] and achieved scalable expansion using a microcarrier system. Second, we fabricated a cell-supporting interface [chlorogenic acid/poly-L-lysine-modified pristine nanofibrous membrane (CA/PLL-PNF)] with antioxidant properties and enhanced hemocompatibility via the layer-by-layer self-assembly of PLL and CA onto polyacrylonitrile nanofibrous membranes. Finally, we assembled these components into a flat-plate bioreactor and evaluated its extracorporeal performance in a Bama miniature pig model after bilateral nephrectomy.**

Results: **iRTECs were stably expanded on microcarriers while maintaining a proximal tubule phenotype, and these cells outperformed existing cell lines in terms of amino acid hydrolysis and transmembrane transport, acid–base regulation, water transport, and endocrine responsiveness. With respect to the supporting interface, CA/PLL-PNF effectively scavenged diverse free radicals and mitigated cellular oxidative stress. Proteomic analysis confirmed that this modification remodeled the plasma protein corona, which significantly reduced the adsorption of complement and coagulation factors. In the bilaterally nephrectomized pig model, the RAD safely maintained extracorporeal circulation for 4 h—the duration of routine clinical dialysis—and preserved internal homeostasis. The antioxidant interface significantly attenuated circulating lipid peroxidation during treatment. Compared with hemofiltration alone, the RAD significantly enhanced the clearance of middle-molecule toxins (β_2-microglobulin) and reduced proinflammatory cytokine levels at the outlet, demonstrating its capacity for the active modulation of local inflammation.**

Received: 25 March 2026. **Revised:** 17 May 2026. **Accepted:** 17 May 2026
© The Author(s) 2026. Published by Oxford University Press.
This is an Open Access article distributed under the terms of the Creative Commons Attribution-NonCommercial License (https://creativecommons.org/licenses/by-nc/4.0/), which permits non-commercial re-use, distribution, and reproduction in any medium, provided the original work is properly cited. For commercial re-use, please contact reprints@oup.com for reprints and translation rights for reprints. All other permissions can be obtained through our RightsLink service via the Permissions link on the article page on our site—for further information please contact journals.permissions@oup.com.

Downloaded from academic.oup.com/burnstrauma/article/doi/10.1093/burnst/tkag036/8687358 by guest on 12 October 2026

Conclusions: **This study established a renal support platform that integrates viable cells and functional materials. The device exhibited multidimensional biological efficacy in toxin clearance and internal homeostasis regulation and achieved stable extracorporeal circulation in a preclinical large animal model, which provides experimental evidence for advanced organ support strategies in the setting of severe AKI.**

Keywords Acute kidney injury, Bioartificial kidney, Renal tubular epithelial cells, Renal assist device, hemocompatibility, Preclinical evaluation

Highlights

- An immortalized human proximal tubule cell line [immortalized renal tubular epithelial cell line (iRTEC)] established by SV40 *Large T* transduction demonstrated preserved brush border enzyme activity, ammoniagenesis, aquaporin-mediated water transport, and parathyroid hormone responsiveness, and was scalably expanded via a 3D microcarrier–spinner flask system.
- A functionalized antioxidant nanofibrous membrane [chlorogenic acid/poly-L-lysine-modified pristine nanofibrous membrane (CA/PLL-PNF)] was fabricated via layer-by-layer self-assembly of CA and PLL onto polyacrylonitrile fibers, which exhibited broad-spectrum radical scavenging, cytoprotection against hydrogen peroxide-induced oxidative stress, and remodeling of the plasma protein corona to reduce complement and coagulation factor adsorption.
- A modular computer numerical control-machined polycarbonate flat-plate bioreactor was developed as a tunable engineering platform, and comprehensive leachable screening confirmed the absence of detectable organic and inorganic toxicants.
- In a bilaterally nephrectomized Bama miniature pig model, compared with hemofiltration alone, the integrated renal tubule assist device maintained safe extracorporeal circulation for 4 h and significantly enhanced β_2-microglobulin clearance (area under the curve: $P = 0.018$).
- The CA/PLL-PNF antioxidant interface attenuated extracorporeal circulation–induced lipid peroxidation *in vivo* (significantly lower circulating malondialdehyde concentration at 4 h; $P = 0.014$), and the cellular component drove a sustained reduction in proinflammatory granulocyte colony-stimulating factor across the device ($P < 0.05$), which demonstrates biological support beyond passive filtration.

Background

Trauma- and critical illness-associated acute kidney injury (AKI) is a severe complication encountered in intensive care units (ICUs). The incidence of AKI among ICU patients ranges from 20% to 50%, with even higher rates observed in severe burn patients [1, 2]. AKI not only directly impairs renal function but also triggers distant organ damage through mechanisms such as fluid imbalance, metabolic waste accumulation, and immune dysregulation, thereby significantly increasing mortality and length of hospital stay [3, 4]. Although blood purification technologies, such as continuous renal replacement therapy (CRRT), have been widely applied in recent decades, AKI-related mortality in the ICU remains high [5].

A primary limitation of existing blood purification technologies is that conventional physical separation only passively removes small-molecule solutes and regulates volume overload and thus fails to replace the biological functions of renal tubular epithelial cells (RTECs) in active transport, acid–base balance, and endocrine homeostasis [6, 7]. Proximal tubular cells, the most abundant cell type in the kidney, are responsible for most water and solute reabsorption. They also drive glutamine metabolism for ammoniagenesis, respond to parathyroid hormone (PTH) signaling, and regulate the synthesis of various cytokines [8, 9]. Consequently, the integration of viable RTECs into extracorporeal circuits—in series with conventional hemofiltration devices to form a bioartificial kidney (BAK)—represents a potential pathway for achieving comprehensive renal functional support [10, 11].

However, further clinical translation of this strategy faces severe challenges because of the lack of stable cell sources and optimized material interfaces. At the seed cell level, human kidney-2 (HK-2) cells, which are currently the most widely used human proximal tubule (PT) cell line (immortalized by the HPV 16 *E6/E7* gene [12]), are highly sensitive to culture conditions. Studies indicate that prolonged passaging of HK-2 cells results in decreased expression of key transporter proteins, which leads to a failure to maintain the essential phenotype required for renal tubular function [13, 14]. Wilmer *et al.* established a conditionally immortalized proximal tubule cell line (ciPTEC) using a dual-gene strategy (SV40 *Large T* and *hTERT*) that showed positive results in transporter function evaluations [15, 16]; however, the conditional system requires temperature switching between permissive (33°C) and nonpermissive (37°C) conditions, which increases the complexity of culture operations. Although they are closer to the *in vivo* state, primary renal tubular cells are constrained by limited availability, significant individual variability, and restricted expansion capacity [17]. Therefore, obtaining a seed cell system that maintains a stable functional phenotype, permits large-scale expansion, and is operationally straightforward remains a critical bottleneck in the field.

The material interfaces that support functional renal tubular cells also present multiple limitations. Traditional hollow-fiber semipermeable membranes used in BAKs serve primarily as passive substrates for cell adhesion and immunoisolation barriers and lack intrinsic bioactivity [10, 18]. However, trauma and severe AKI are frequently accompanied by elevated systemic oxidative stress and uncontrolled inflammatory responses [19]. Cells within the device are simultaneously exposed to multiple detrimental factors during extracorporeal circulation, including uremic toxins, shear stress, and reactive oxygen species (ROS). Furthermore, protein adsorption, complement activation, and coagulation cascades triggered by blood/plasma-material contact

Downloaded from academic.oup.com/burnstrauma/article/doi/10.1093/burnst/tkag036/8687358 by guest on 12 October 2026

represent core safety concerns for extracorporeal devices [20, 21]. Recently, electrospun nanofibrous membranes have attracted widespread attention in tissue engineering because of their high surface-to-volume ratio and extracellular matrix-like topography [22, 23]. Layer-by-layer (LbL) assembly techniques, characterized by mild conditions and controllable stratification, have been employed for surface functionalization [24]. Nevertheless, studies utilizing antioxidant-functionalized nanofibrous membranes as a cell-supporting interface for renal tubular cells, alongside systematic evaluations of their hemocompatibility and protein corona profiles, remain scarce.

At the bioreactor level, traditional hollow-fiber-based renal tubule assist devices (RADs) rely on commercial filters with preconfigured structural parameters (e.g. inner diameter, wall thickness, and membrane area). Custom modifications during the research and development phase require costly and time-consuming remanufacturing [10, 25]. In contrast, flat-plate structures fabricated via computer numerical control (CNC) machining or 3D printing offer well-defined flow channels, facilitate straightforward membrane coating and live-cell sampling, and better accommodate the rapid iteration demands of preclinical development [26, 27].

To address these limitations, this study aims to establish a comprehensive preclinical development and evaluation framework that spans seed cell preparation, material interface functionalization, modular bioreactor design, and large animal *in vivo* validation (Figure 1). In the first phase, we established an immortalized human proximal tubule cell line, immortalized renal tubular epithelial cell line (iRTEC), via SV40 *Large T* lentiviral transduction of primary cells, achieved large-scale expansion using a microcarrier-based spinner flask system, and systematically validated its morphology, phenotype, and multidimensional physiological functions. In the second phase, using polyacrylonitrile (PAN) electrospun nanofibrous membranes as a base, we fabricated a functionalized, antioxidant cell-supporting interface via the LbL self-assembly of chlorogenic acid (CA) and poly-L-lysine (PLL). This interface was thoroughly evaluated for its physicochemical properties, antioxidant performance, hemocompatibility, and protein corona proteomics. In the third phase, we custom-designed a CNC-machined polycarbonate multilayer flat-plate bioreactor and verified its safety. Finally, we integrated the RAD device with a hemofiltration circuit in a Bama miniature pig model of acute renal failure, in which the pigs underwent bilateral nephrectomy, to evaluate its safety and biological support functionality during a 4-h period of extracorporeal circulation.

Methods

Establishment of the immortalized human proximal tubule cell line

Primary cell isolation and culture

Approval for this study was obtained from the Ethics Committee of the Chinese PLA General Hospital (S2022-640-01). Human kidney tissue was collected from patients undergoing nephrectomy with informed consent. Immediately after surgery, cortical tissue ($\sim$1 cm^3) was excised from the pole distant from the tumor, placed in prechilled preservation buffer at 4°C, and transported to the laboratory. After the renal capsule and residual medulla were removed, the tissue was minced into $\sim$3 mm^3 pieces and passed through sequential 80- and 150-mesh sieves to enrich for tubular fragments. The fragments were digested with TrypLE Express (Gibco) at 37°C for $\sim$20 min, followed by centrifugation at $100 \times g$ for 5 min. The pelleted cells were seeded in T-25 flasks with DMEM/F12 complete medium (10% FBS, 1% penicillin–streptomycin) and cultured at 37°C in 5% CO_2. The medium was first replaced 24 h after seeding to remove nonadherent cells and erythrocytes.

Lentiviral transduction and drug selection

A lentiviral expression vector, plv-cmv-Large T-pgk-BSD (the CMV promoter driving SV40 *Large T*; the PGK promoter driving the blasticidin resistance gene), was utilized. 293 T cells were cotransfected at a plasmid ratio of 3:2:1 (plv-cmv-Large T-pgk-BSD: psPAX2: pMD2.G). Viral supernatant was collected 48–72 h posttransfection and filtered (0.45 μm). Primary cells were infected for 24 h with viral supernatant diluted in culture medium (7:3 ratio) supplemented with 10 μg/mL polybrene. After 48 h, the cells were subjected to selection with blasticidin (12.0 μg/mL) for $\sim$10 days to establish the iRTEC line.

Immortalized renal tubular epithelial cell line characterization and functional validation

Phenotypic characterization

Large T mRNA expression was quantified via reverse transcription quantitative polymerase chain reaction (RT–qPCR) (18S rRNA internal control; primers in Table S1). Apical surface morphology was examined using scanning electron microscopy (SEM; detailed protocol in the Supplementary file). Proliferative stability was assessed by comparing the population doubling times across passages P2–P4.

Functional evaluation

(i) To determine GGT activity, 4×10^6 cells were sonicated, after which the supernatant was assayed using a γ-glutamyl transpeptidase (GGT) assay kit (Elabscience, E-BC-K126-M). The activity was normalized to the number of cells (U/10^4 cells) and compared to that of HK-2 cells. (ii) Ammonia production: following a 4 h incubation at a standardized seeding density, the supernatant was quantified using an ammonia assay kit (Sigma–Aldrich, MAK310), with HK-2 as a control. (iii) water transport function (calcein-AM hypo-osmotic fluorescence decay assay): cells loaded with 1.6 μM calcein-AM were subjected to a 0.06% NaCl hypo-osmotic stimulus. Kinetic fluorescence (Ex 485 nm/Em 520 nm) was recorded (0–270 s) using a Tecan Spark microplate reader and normalized to the 0 s baseline (100%), after which the AUC was calculated. HK-2 served as a control. (iv) PTH responsiveness: The cells were stimulated with PTH (100 nmol/L) for 30 min in the presence of IBMX. Following lysis, intracellular cAMP levels were quantified using a cAMP Parameter kit (R&D Systems, KGE002B) and are expressed as pmol/mg protein.

Microcarrier-based large-scale expansion

Prewetted 3D TableTrix® microcarriers and iRTECs were introduced into 500 mL spinner flasks (initial working volume: 125 mL). During the attachment phase (0–24 h), intermittent

Downloaded from academic.oup.com/burnstrauma/article/doi/10.1093/burnst/tkag036/8687358 by guest on 12 October 2026

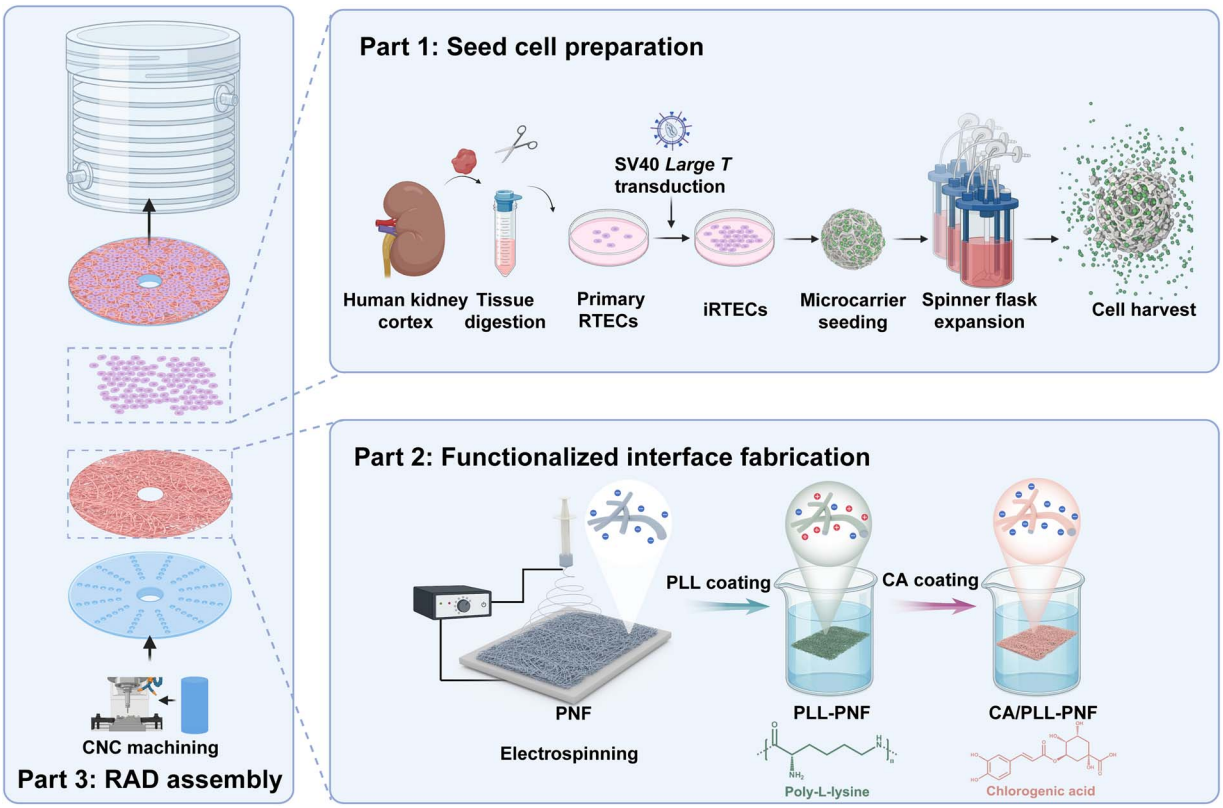


Figure 1 Schematic illustration of the construction and evaluation strategy for an RAD that integrates viable cells and a functionalized LbL assembled interface. The RAD was developed across three core modules. Part 1: primary RTECs were isolated from the human renal cortex and immortalized via SV40 *Large T* lentiviral transduction to establish an iRTEC line, which demonstrated a preserved PT functional phenotype and was scalably expanded using a microcarrier-based spinner flask system. Part 2: PAN electrospun nanofibrous membranes (PNF) were sequentially modified with PLL and CA via LbL assembly to fabricate the functionalized CA/PLL-PNF interface. Part 3: a polycarbonate multilayer flat-plate bioreactor was CNC-machined. The CA/PLL-PNF interface was coated onto culture discs, seeded with iRTECs, and stacked to assemble the complete RAD for subsequent large-animal extracorporeal circulation validation. An experimental scheme was generated using BioRender.com with a license. *iRTEC* immortalized renal tubular epithelial cell line, *PNF* pristine polyacrylonitrile nanofibrous membrane, *CA/PLL-PNF* chlorogenic acid and poly-L-lysine sequentially modified PNF

low-speed stirring (30 rpm; 5 min on/25 min off) was applied, alongside a control subjected to continuous stirring. Attachment rate = $(1 - Ns/Ni) \times 100\%$. After 24 h, the culture transitioned to continuous stirring (35 rpm) for dynamic expansion, and 50% of the medium was exchanged every other day. The cell number and glucose and lactate concentrations were monitored daily. Flow cytometry (FlowJo software) was used to analyze CD13, CD10, and Ki67 expression before and after expansion. Intact microcarrier–cell complexes were cryopreserved using a controlled-rate freezer (Table S2). Postthaw viability (at 3 and 7 days) was determined via Trypan blue exclusion following rapid thawing in a 37°C water bath.

Preparation and characterization of chlorogenic acid/poly-L-lysine-modified pristine nanofibrous membrane

Membrane preparation

PAN (3 g) was dissolved in DMF (20 g) and electrospun (16 kV, 18 cm, 6 h) to fabricate the pristine nanofibrous membrane (PNF), which was dried at 80°C. PNF was immersed in a PLL solution (1 g/500 mL H_2O) for 8 h to yield PLL-PNF; subsequently, PLL-PNF was immersed in a CA solution (1 g/500 mL H_2O) for 8 h to obtain CA/PLL-PNF. Each step was followed by thorough washing and drying at 60°C.

Physicochemical characterization

Fiber morphology and diameter distribution were evaluated via SEM (ImageJ). Stepwise chemical modifications were verified by Fourier-transform infrared spectroscopy (FTIR). The surface elemental composition was analyzed by X-ray photoelectron spectroscopy (XPS; Al Kα and C 1 s 284.8 eV calibrations). The surface charge (ζ potential at pH $\approx$ 7.4), wettability (static water contact angle, WCA), and thermal stability [thermogravimetric analysis/derivative thermogravimetry (TGA/DTG)] were evaluated. Tensile testing (50 mm/min), liquid saturation porosity, and dead-end pure water flux were also measured.

Antioxidant performance evaluation

Chemical radical scavenging activity was assessed using the 2,2-diphenyl-1-picrylhydrazyl (DPPH), 2,2′-azino-bis(3-ethylbenzothiazoline-6-sulfonic acid) (ABTS), and 2-phenyl-4,4,5,5-tetramethylimidazoline-1-oxyl 3-oxide (PTIO) systems. Physiological ROS clearance was evaluated using superoxide anion and hydrogen peroxide (H_2O_2) assays. Following membrane immersion, clearance rates were calculated according to the changes in absorbance using a ultraviolet–visible (UV–Vis) spectrophotometer.

Downloaded from academic.oup.com/burnstrauma/article/doi/10.1093/burnst/tkag036/8687358 by guest on 12 October 2026

Hemocompatibility evaluation: hemolysis

Membranes were incubated with a 2% erythrocyte suspension at 37°C for 3 h; hemolysis rates were calculated according to the absorbance at 540 nm. "Complete blood count and coagulation": Whole blood or platelet-poor plasma (PPP) was incubated with the membranes for 1 h at 37°C to measure hematological parameters and APTT, PT, TT, and FIB. Blood cell adhesion was observed by SEM. Nonspecific protein adsorption was quantified by confocal microscopy using BSA-FITC (0.25 mg/mL, 1 h). "Complement activation": complement component 3a (C3a) and soluble C5b-9 (terminal complement complex) (sC5b-9) levels were measured by enzyme-linked immunosorbent assay (ELISA) following membrane-plasma incubation.

Cytocompatibility and oxidative stress protection

Cells treated with membrane extracts (3 cm^2/mL, 37°C for 24 h; ISO 10993-12) were analyzed for apoptosis using flow cytometry-based Annexin V-FITC/PI staining. Cytoskeletal spreading was visualized via F-actin/DAPI staining after 24 h of culture on the membranes. In the H_2O_2-induced oxidative stress model (200 μM, 4 h), intracellular ROS levels were quantified using a 2′,7′-dichlorodihydrofluorescein diacetate (DCFH-DA) probe and flow cytometry. Flow cytometry data acquisition for Annexin V-FITC/PI apoptosis assays and DCFH-DA-based intracellular ROS measurements was performed with technical support from Tianjin Jinke Biotechnology Co., Ltd.

Protein corona proteomics

Plasma for these experiments was obtained, with informed consent, from healthy donors and from patients with AKI and CKD under the same ethics approval. Membranes (0.8 cm diameter) were prewetted in PBS for 1 h and then incubated with 0.5 mL of human plasma at 37°C in the dark for 1 h. After the weakly bound proteins were removed, the membrane-associated proteins were extracted, reduced with DTT, alkylated with iodoacetamide, and digested overnight in trypsin. Following C18 desalting, the peptides were analyzed via liquid chromatography-tandem mass spectrometry (LC–MS/MS) (Q Exactive HF, DDA mode; Table S3). Differentially abundant proteins were defined by $|\log_2 FC| > 0.58$ and $P < 0.05$. Gene Ontology (GO) and Kyoto Encyclopedia of Genes and Genomes (KEGG) enrichment analyses were performed using bioinformatics.com.cn.

Bioreactor design and biosafety validation

Design and fabrication

A modular, multilayer flat-plate bioreactor was designed using parameterized CAD and was CNC-machined from polycarbonate (Figure S1). The core components include a cylindrical housing, a threaded lid with a VMQ O-ring, positioning pillars, and culture discs (72 evenly distributed 1.5 mm pores). The CA/PLL-PNF nanofibrous layer was directly electrospun onto the culture discs (Figure S2 and S3). "Biosafety validation": comprehensive screening for leachables such as VOCs, SVOCs, NVOCs, inorganic elements (ICP, >70 elements), and inorganic anions (IC) was performed. Hemolysis and hematological toxicity were also evaluated.

Extracorporeal circulation in the Bama miniature pig acute kidney injury model

Animal model and setup

All animal procedures were approved by the institutional Ethics Committee and performed in line with institutional guidelines for laboratory animal care. Six healthy Bama miniature pigs (23 ± 2.17 kg) were anesthetized and intubated, after which anesthesia was maintained with isoflurane (2%). Bilateral nephrectomy was performed via a midline abdominal incision. Expanded iRTECs were dissociated using modified detachment buffer (100 U/mL DNase I, 10 μM Y-27632) and seeded onto collagen IV-coated CA/PLL-PNF culture discs. Following overnight attachment, the discs were assembled into the bioreactor, sealed, and transported. "Extracorporeal circulation": at 24 h postsurgery, the animals were randomized into the RAD ($n = 3$) and No-RAD ($n = 3$) groups. Ultrasound-guided subclavian vein catheterization was then performed. The primary hemofiltration circuit operated at Qb = 130 mL/min. In the RAD group, a plasma separation branch was arranged in parallel: separated plasma was perfused through the RAD using a peristaltic pump (30 mL/min) before it was rejoined to the venous return. The system was operated for 4 h under systemic heparinization (Figure S4; Table S4). "Monitoring and detection": blood was sampled every hour. Blood gasses and electrolytes (pH, PCO_2, HCO_3^-, BEecf, Na^+, K^+) were monitored using a portable clinical analyzer (i-STAT 300G; Abbott). Serum biochemical parameters, including hepatic enzymes (ALT and AST), cardiac injury markers (CK and CK-MB), lactate dehydrogenase (LDH), C-reactive protein (CRP), renal function markers [creatinine, urea, β_2-microglobulin (β_2-MG), and cystatin C], and oxidative stress-related indicators [malondialdehyde (MDA), glutathione reductase (GR), and catalase (CAT)], were measured using an automated biochemical analyzer (TBA-120FR, Toshiba). Plasma samples collected from the RAD inlet and outlet at 2 h and 4 h were used to quantify interleukin-6 (IL-6), interleukin-10 (IL-10), and granulocyte colony-stimulating factor (G-CSF) using porcine-specific ELISA kits (Porcine IL-6, #P6000B; Porcine IL-10, #P1000B; Porcine G-CSF/CSF3, #PCG00; R&D Systems, Minneapolis, MN, USA).

Statistical analysis

Data were analyzed using SPSS 26.0 and GraphPad Prism 10 and are expressed as the mean ± standard deviation (SD). Normality and homoscedasticity were assessed using the Shapiro–Wilk and Levene tests, respectively; all datasets met both assumptions ($P > 0.05$), and parametric tests were therefore applied for all analyses. For multigroup comparisons, one-way analysis of variance (ANOVA) followed by Bonferroni post hoc correction was used. Two-group comparisons were performed using the independent-samples *t* test. For longitudinal data involving two groups across multiple time points, two-way repeated-measures ANOVA was applied; when a significant time × group interaction was detected, post hoc pairwise comparisons were performed using Šidák's correction. The area under the curve (AUC) was calculated using the trapezoidal rule. A two-tailed $P < 0.05$ indicated statistical significance.

Downloaded from academic.oup.com/burnstrauma/article/doi/10.1093/burnst/tkag036/8687358 by guest on 12 October 2026

Results

Establishment, functional characterization, and scalable production of the immortalized renal tubular epithelial cell line

Establishment and characterization of the immortalized renal tubular epithelial cell line

To obtain seed cells capable of stable expansion while preserving proximal tubule (PT) functions, we established an immortalized cell line, iRTEC, via lentiviral transduction of SV40 Large T antigen into primary human RTECs. Following transduction and blasticidin-based selection, uninfected control cells underwent complete cell death within 5 days, whereas the surviving infected cells gradually resumed proliferation, resulting in the formation of a morphologically uniform and stable iRTEC population. RT–qPCR confirmed the high expression of *Large T* mRNA in iRTECs (Fig. 2b, $P < 0.0001$). The population doubling times across passages P2–P4 were not significantly different (Fig. 2c, ns), indicating robust proliferative stability. SEM revealed that iRTECs formed a continuous, well-spread epithelial monolayer on the substrate, characterized by apical microvilli and ridge-like microstructures (Fig. 2d).

Immortalized renal tubular epithelial cell lines retain brush border metabolic and transport functions

After the iRTEC line was established, we systematically evaluated its PT functionality across four dimensions: brush border enzyme activity, nitrogen metabolism, transmembrane water transport, and endocrine signal responsiveness. GGT, a signature brush border enzyme of PT cells, catalyzes the hydrolysis of extracellular glutathione to release cysteine and glycine for cellular reutilization while participating in transmembrane amino acid transport. Its activity directly reflects the differentiation and maturation of the apical brush border in PT epithelial cells [28]. The GGT activity of iRTECs was 0.3220 ± 0.0531 U/10^4 cells, which was >20-fold greater than that of HK-2 cells (0.0152 ± 0.0018 U/10^4 cells) (Fig. 2g, $P < 0.001$), demonstrating that iRTECs retain a more mature brush border phenotype and amino acid metabolic capacity.

Immortalized renal tubular epithelial cell lines possess an acid–base regulatory functional reserve

In addition to brush border enzyme activity, ammoniagenesis serves as another critical indicator of preserved metabolic function in PT cells. To assess the acid–base regulatory potential of iRTECs, we measured the *in vitro* ammonia production in these cells. Renal ammoniagenesis occurs almost exclusively in the PT, primarily via glutamine deamination. This represents a fundamental physiological mechanism for the maintenance of systemic acid–base homeostasis; in response to a decreased environmental pH, the PT compensates by upregulating ammonia production [29]. Therefore, cellular ammonia production directly reflects the presence of metabolic pathways required for systemic acid–base regulation. The ammonia production in iRTECs was 2.635 ± 0.174 μg/mg, which was significantly greater than that in HK-2 cells (1.306 ± 0.0714 μg/mg) (Fig. 2e, $P < 0.001$), confirming that iRTECs possess a superior functional reserve for acid–base regulation.

Immortalized renal tubular epithelial cell lines maintain aquaporin-mediated water transport function

To evaluate transport capacity, we employed a calcein-AM hypo-osmotic fluorescence decay assay to measure water transport function. The PT is responsible for reabsorbing ~65% of the water from the glomerular filtrate. This high-capacity water transport depends on the expression of high levels of aquaporins on the cell membrane [30]. Osmotic loading assays evaluate whether these aquaporins facilitate functional mass exchange, thereby reflecting the maintenance of cellular polarity. During the hypo-osmotic challenge, the fluorescence decay rate of iRTECs was markedly faster than that of HK-2 cells, with a significantly lower AUC from 0 to 270 s ($12\,864.5 \pm 148.5\%\cdot s$ *vs* $16\,324.5 \pm 63.5\%\cdot s$) (Fig. 2h), which confirms the preservation of aquaporin-mediated transmembrane water transport.

Immortalized renal tubular epithelial cell lines preserve endocrine signal responsiveness to parathyroid hormone

To evaluate the capacity of iRTECs to sense and respond to endocrine signals, we measured changes in intracellular cAMP levels following PTH stimulation. Under physiological conditions, the parathyroid gland regulates blood calcium and phosphate levels through the secretion of PTH. Upon reaching the kidney, PTH triggers enzymatic cascades (e.g. protein kinase A activation) that increase the level of intracellular cAMP in PT cells, which regulates calcium and phosphate reabsorption [31]. Thus, a functional cAMP response provides direct biochemical evidence of the potential of these cells to participate in systemic fluid and electrolyte regulation. Following stimulation with 100 nmol/L PTH, the level of intracellular cAMP in iRTECs increased ~57-fold, from 0.2633 ± 0.0950 pmol/mg to 14.91 ± 3.074 pmol/mg (Fig. 2f $P < 0.01$), which confirms that the PTH1R → Gs → cAMP signaling axis remained intact and highly active.

Stable, large-scale expansion via a microcarrier system

To meet the cellular demands for the operation of BAK devices, we established a dynamic spinner-flask expansion system based on 3D microcarriers and systematically evaluated expansion efficiency, phenotypic stability, and the feasibility of cryopreserving intact microcarrier-cell complexes. In a 500 mL spinner-flask system, compared with the continuous stirring group, the intermittent stirring group exhibited significantly higher cell attachment rates at 4 h and 8 h (4 h: $64.30 \pm 1.65\%$ *vs* $53.70 \pm 1.80\%$, $P < 0.05$; 8 h: $75.87 \pm 1.85\%$ *vs* $66.97 \pm 1.20\%$, $P < 0.05$), and both groups converged at 24 h (Figure S5). Live/dead fluorescence staining demonstrated high cell viability throughout the 3D dynamic culture (Fig. 2i). Quantification revealed that the total cell number increased from $1.00 \pm 0.07 \times 10^6$ on day 0 to $12.17 \pm 1.05 \times 10^6$ on day 6, which indicates ~12-fold expansion (Fig. 2j–k). Concurrent metabolic monitoring revealed a continuous decrease in glucose (24.03 to 12.80 mM) coupled with a synchronous increase in lactate (1.23 to 9.70 mM) (Fig. 2l and m), indicating an active metabolic state. Confocal microscopy revealed that the DAPI (blue), F-actin (green), and DiI (red) signals intensified over the culture period

Downloaded from academic.oup.com/burnstrauma/article/doi/10.1093/burnst/tkag036/8687358 by guest on 12 October 2026

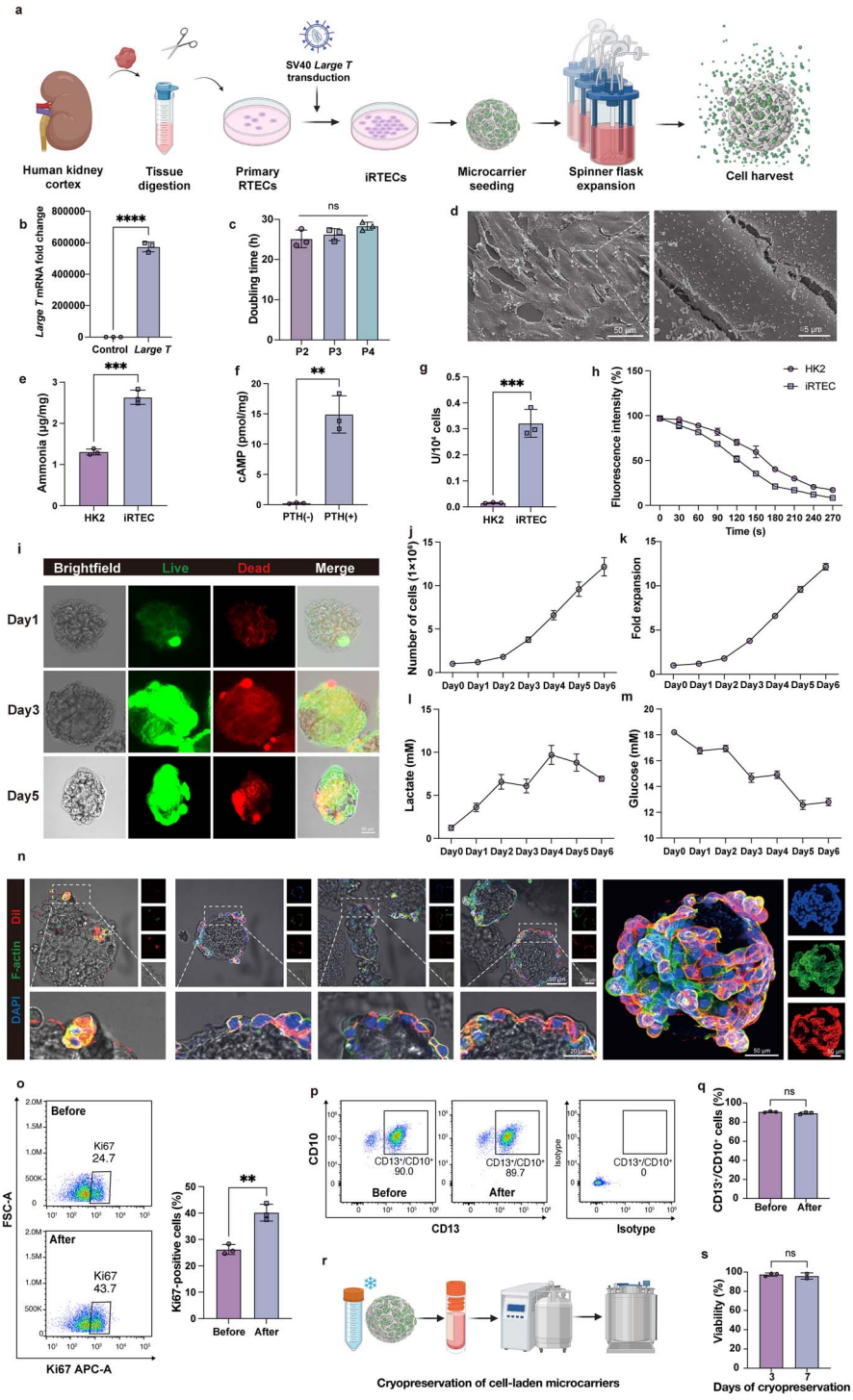


Figure 2 Establishment, functional characterization, and microcarrier-based expansion of the iRTEC. (**a**) Overall experimental pipeline. An image showing the experimental scheme was generated using BioRender.com with a license. (**b**) Relative *Large T* mRNA expression detected by RT–qPCR (****$P < 0.0001$). (**c**) Population doubling times of iRTECs across passages P2–P4 (ns). (**d**) SEM image of iRTECs showing epithelial spreading and apical microvilli. (**e**) *In vitro* ammonia production in iRTECs compared with that in HK-2 cells (***$P < 0.001$). (**f**) Intracellular cAMP levels before and after PTH stimulation (**$P < 0.01$). (**g**) Quantification of GGT activity (***$P < 0.001$). (**h**) Kinetic fluorescence decay curves for aquaporin-mediated water transport using the calcein-AM hypo-osmotic assay. (**i**) Live/dead fluorescence and brightfield imaging of cell-loaded microcarriers during dynamic 3D culture. (**j**–**k**) Growth curve of total cell number (j) and expansion fold change (k). (**l**–**m**) Metabolic monitoring showing increasing lactate (l) and decreasing glucose (m) concentrations over time. (**n**) Confocal imaging of cell-loaded microcarriers (DAPI, blue; F-actin, green; DiI, red). (**o**) Flow cytometric analysis and quantification of Ki67 expression before and after expansion (**$P < 0.01$). (**p**–**q**) Flow cytometric analysis of CD13 and CD10 coexpression before and after expansion. (p) Representative dot plots. (q) Quantification of the percentage of $CD13^+CD10^+$ cells, which did not significantly differ after expansion (ns). (**r**–**s**) Schematic of the programmable cryopreservation strategy for intact microcarrier–cell complexes (r) and postthaw viability at different time points (s) (ns). Statistical significance was assessed by independent-samples *t* tests (two-group comparisons) or one-way ANOVA with Bonferroni correction (multigroup comparisons); *$P < 0.05$, **$P < 0.01$, ***$P < 0.001$, ****$P < 0.0001$. *RT–qPCR* reverse transcription quantitative polymerase chain reaction, *cAMP* cyclic adenosine monophosphate, *calcein-AM* calcein-acetoxymethyl ester, *DAPI*4′,6-diamidino-2-phenylindole, *DiI* 1,1′-dioctadecyl-3,3,3′,3′-tetramethylindocarbocyanine perchlorate, *CD* cluster of differentiation, *ANOVA* analysis of variance, *ns* not significant

Downloaded from academic.oup.com/burnstrauma/article/doi/10.1093/burnst/tkag036/8687358 by guest on 12 October 2026

as the cells adhered, spread, and formed microtissues on the microcarrier surface (Fig. 2n).

Flow cytometry revealed a significant increase in the Ki67-positive rate after expansion (25.4% *vs* 44.7%, $P < 0.01$) (Fig. 2o). In contrast, no significant difference was observed in the proportion of $CD13^{+}CD10^{+}$ cells before and after expansion (Fig. 2p and q; ns), which suggests that the expansion process did not markedly alter the epithelial-associated proximal tubular phenotype of the cells.

To enable a rapid, on-demand supply of seed cells, we evaluated the programmable cryopreservation of intact microcarrier–cell complexes. This approach allows thawed cells to be directly inoculated into spinner flasks, bypassing the initial attachment phase. Following cryopreservation using a controlled-rate freezer for 3 and 7 days, the postthaw viability of the cells on the carriers remained ≥95% (Fig. 2s). These findings indicate that microcarrier-bound cells can tolerate programmable cryopreservation without significant loss of viability, offering a practical strategy for the rapid initiation of cell expansion.

Construction and safety evaluation of the functionalized cell-supporting interface and device module

Physicochemical characteristics of the chlorogenic acid/poly-L-lysine-modified pristine nanofibrous membrane

To engineer an optimal cell-supporting interface for functional PT cells—and to address the limitations of conventional substrates, which lack bioactivity and frequently trigger complement activation and coagulation upon blood contact—we fabricated a functionalized CA/PLL-PNF membrane via the LbL self-assembly of PLL and CA onto a PAN nanofibrous membrane. SEM revealed that all three membrane groups maintained a typical nonwoven nanofibrous network, with a shift toward larger fiber diameters following stepwise modification (Fig. 3b–d). FTIR spectroscopy confirmed the successful introduction of PLL, as evidenced by new absorption peaks at 1666 cm^{-1} (amide I) and 1529 cm^{-1} (amide II), whereas the subsequent addition of CA introduced characteristic peaks at 3361 cm^{-1} (–OH) and 1254/1175 cm^{-1} (C–O) (Fig. 3e). XPS analysis revealed that the percentage of oxygen in the CA/PLL-PNF increased from 3.50% to 25.87% and that high-resolution spectra displayed characteristic O–C=O and $-NH_3^{+}$ peaks (Fig. 3f; Table S5). The TGA/DTG curves exhibited three-stage thermal degradation behavior (Fig. 3g).

Following modification, the ζ-potential exhibited a dynamic shift of $-158 \rightarrow -45 \rightarrow -79$ mV (Fig. 3h), the water contact angle (WCA) decreased from 98.03° to 42.77° (Fig. 3i), and the volumetric porosity was maintained at 81% (Fig. 3j; Table S6). The pure water flux reached 1249.96 L/(m^2·h) (Fig. 3k). Mechanically, the tensile strength increased from 6.09 to 10.95 MPa, and the Young's modulus improved from 76.16 to 159.75 MPa, while the membrane remained flexible and could be folded and restored without damage (Fig. 3l; Table S7; Figure S6).

Antioxidant activity and cytocompatibility of chlorogenic acid/poly-L-lysine-modified pristine nanofibrous membrane

To assess the ability of CA/PLL-PNF to protect against an oxidative microenvironment, we evaluated its radical scavenging activity using both chemical assays and a cellular H_2O_2-induced oxidative stress model. CA/PLL-PNF exhibited a highly efficient scavenging capacity against the chemical radicals DPPH (88.49%) (Fig. 4a and b) and ABTS (71.00%) (Fig. 4c and d) and demonstrated a 45.00% clearance rate against PTIO radicals (Fig. 4e and f). CA/PLL-PNF also demonstrated robust clearance of physiological ROS and achieved an 82.96% superoxide anion clearance rate (Fig. 4g and h) and a 52.08% H_2O_2 clearance rate (Fig. 4i and j). A radar chart comprehensively illustrates the overall superiority of CA/PLL-PNF across these five metrics (Fig. 4k).

After the intrinsic antioxidant activity of the material was confirmed, we further evaluated its biocompatibility and protective efficacy as a cell-supporting interface. F-actin cytoskeletal staining of cells cultured on the membranes revealed more extensive cell spreading in the CA/PLL-PNF group (Fig. 4l). Treatment with the membrane extracts resulted in no significant difference in total apoptosis across the groups (Fig. 4o and p), and no difference in cell viability was observed (Fig. 4q), which indicates the absence of apparent cytotoxicity. In the H_2O_2-induced oxidative stress model, the intracellular ROS levels in the CA/PLL-PNF group were significantly lower than those in the H_2O_2 control group (Fig. 4m and n, $P < 0.0001$), demonstrating that functional modification effectively translated the antioxidant properties of the material into active cytoprotective effects.

Hemocompatibility and protein corona modulation of chlorogenic acid/poly-L-lysine-modified pristine nanofibrous membrane

The hemocompatibility of the material interface directly dictates the operational safety of the device. Accordingly, we evaluated CA/PLL-PNF across four parameters: hemolysis, blood cell response, coagulation, and protein adsorption. Hemolysis assays demonstrated that the hemolysis rates for all three membrane groups were below the 2% threshold recommended by the ISO 10993-4:2017/ASTM F756-17 guidelines (Fig. 5b). No significant differences were observed in the WBC or PLT counts among the groups (Fig. 5c). Coagulation assays revealed no significant differences in PT or TT, whereas APTT differed significantly between the PNF group and the control group ($P < 0.01$) (Fig. 5d). Fibrinogen (FIB) levels did not significantly differ across the groups (Fig. 5e). SEM imaging demonstrated a progressive decrease in both blood cell adhesion and nonspecific BSA adsorption on the CA/PLL-PNF surface (Fig. 5f). The fluorescence intensity of adsorbed BSA-FITC was significantly reduced (Fig. 5g, $P < 0.0001$). ELISA revealed that C3a levels were significantly reduced after CA/PLL-PNF modification (Fig. 5h, $P < 0.0001$), whereas the level of sC5b-9 was not significantly different among the groups (Fig. 5i, ns).

To elucidate the underlying molecular mechanisms of this improved hemocompatibility, we performed LC–MS/MS proteomic analysis of the plasma protein corona formed on the membrane surface. In all, 446 proteins were identified: 226, 258, and 233 proteins were identified in the control (Con, PNF) group, whereas 272, 272, and 293 proteins were identified in the modified (Mat, CA/PLL-PNF) group. The two groups shared 230 proteins, with 60 unique to the Con group and 156 unique to the Mat group (Fig. 5j). A hierarchical clustering ring heatmap revealed clear segregation between the protein corona compositions of the two groups, indicating that surface modification profoundly altered the protein adsorption profile (Fig. 5k). Enrichment analysis revealed that the differentially adsorbed proteins were primarily involved in

Downloaded from academic.oup.com/burnstrauma/article/doi/10.1093/burnst/tkag036/8687358 by guest on 12 October 2026

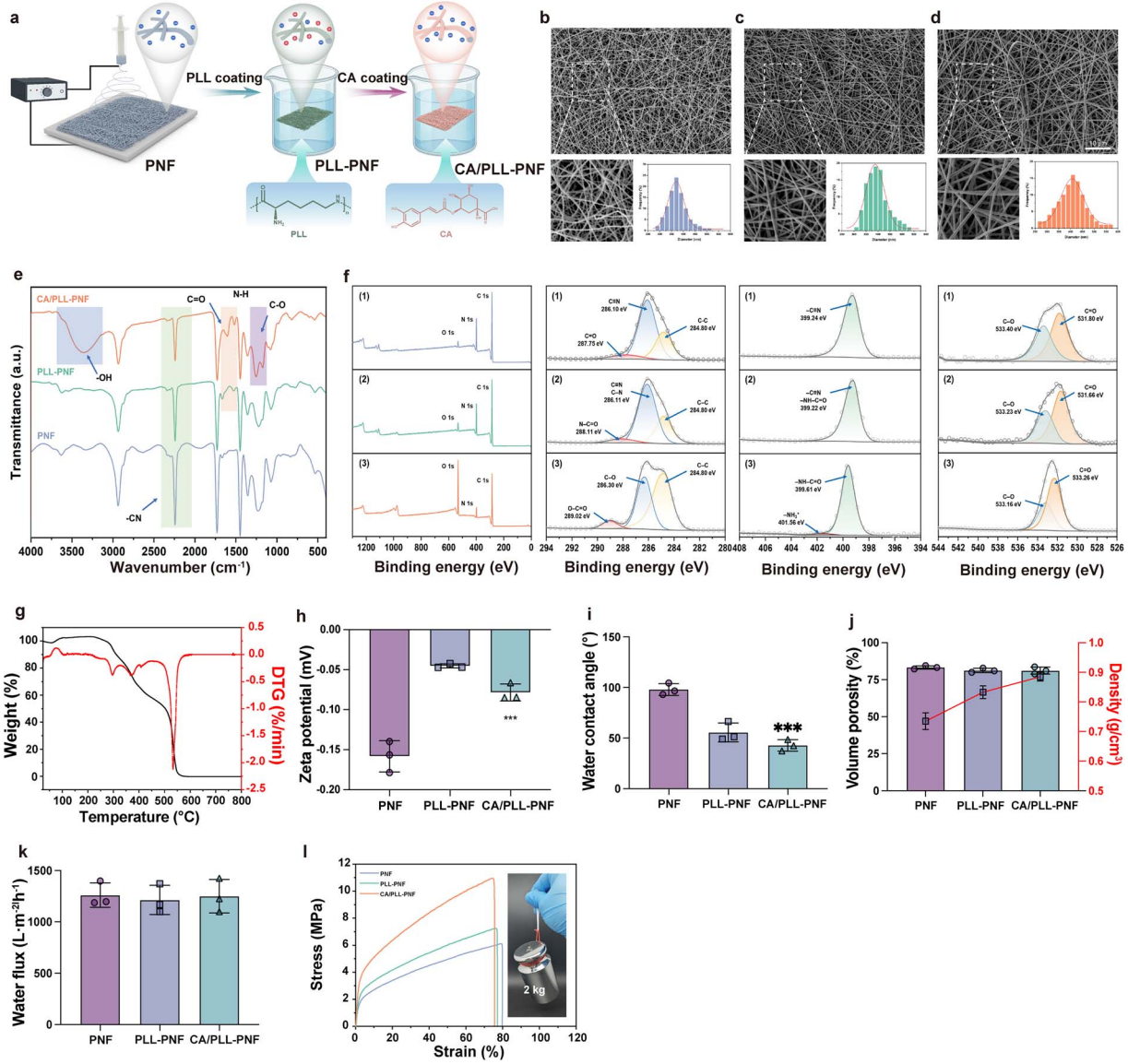


Figure 3 LbL fabrication and physicochemical characterization of the cell-supporting CA/PLL-PNF-functionalized interface. (**a**) Schematic of the LbL assembly process and the chemical structures of PLL and CA. The scheme was generated using BioRender.com with a license. (**b**–**d**) SEM images and fiber diameter distributions of PNF (b), PLL-PNF (c), and CA/PLL-PNF (d). (**e**) FTIR spectra verifying the stepwise chemical modifications. (**f**) Full XPS spectra and high-resolution spectra of C 1 s, N 1 s, and O spectra (1: CA/PLL-PNF; 2: PLL-PNF; 3: PNF). (**g**) TGA and DTG curves for the evaluation of thermal stability. (**h**–**k**) Changes in the surface ζ-potential (h) (***$P < 0.001$), static water contact angle (i) (***$P < 0.001$), volumetric porosity and apparent density (j), and pure water flux (k). (**l**) Tensile stress–strain curves and macroscopic demonstration of membrane flexibility. Statistical significance was assessed by one-way ANOVA with Bonferroni correction; ***$P < 0.001$. *PLL-PNF* poly-L-lysine modified PNF, *ζ-potential* zeta potential

biological processes such as complement cascades, complement regulation, platelet (PLT) degranulation, and lipoprotein particle remodeling (Fig. 5l and m). KEGG analysis further confirmed that complement and coagulation cascades were among the primary enriched pathways (Fig. 5n). A scatter plot of differentially adsorbed proteins revealed a systematic downregulation of complement and coagulation-related proteins—including C6, C1QC, C1QB, CFH, F12, C8G, SERPINC1, C8B, VTN, PROS1, F7, and SERPIND1—within the corona of the Mat group (Fig. 5o). These data demonstrate that the LbL functionalization of CA/PLL-PNF remodels the surface protein corona to reduce the accumulation of complement and coagulation factors, providing a key molecular basis for its ability to mitigate complement activation and enhance hemocompatibility.

Biosafety validation of the computer numerical control-machined bioreactor

Following the preparation of the seed cells and the CA/PLL-PNF interface, we integrated these components into a custom-designed, multilayer polycarbonate flat-plate bioreactor to construct the complete RAD. Prior to animal testing, the biosafety of the bioreactor bulk material was validated. A comprehensive screen for leachables (VOCs, SVOCs, NVOCs, inorganic elements, and IC) was performed (Table S8). ICP screening of >70 inorganic elements revealed that all were below the detection limit, except for trace amounts of common elements (K, Ca, Se, and Br), and that inorganic anion levels (nitrate, sulfate, and phosphate) were comparable to those of the blank control (Table S9). The hemolysis rate was only 0.084%, well below the 2% threshold described

Downloaded from academic.oup.com/burnstrauma/article/doi/10.1093/burnst/tkag036/8687358 by guest on 12 October 2026

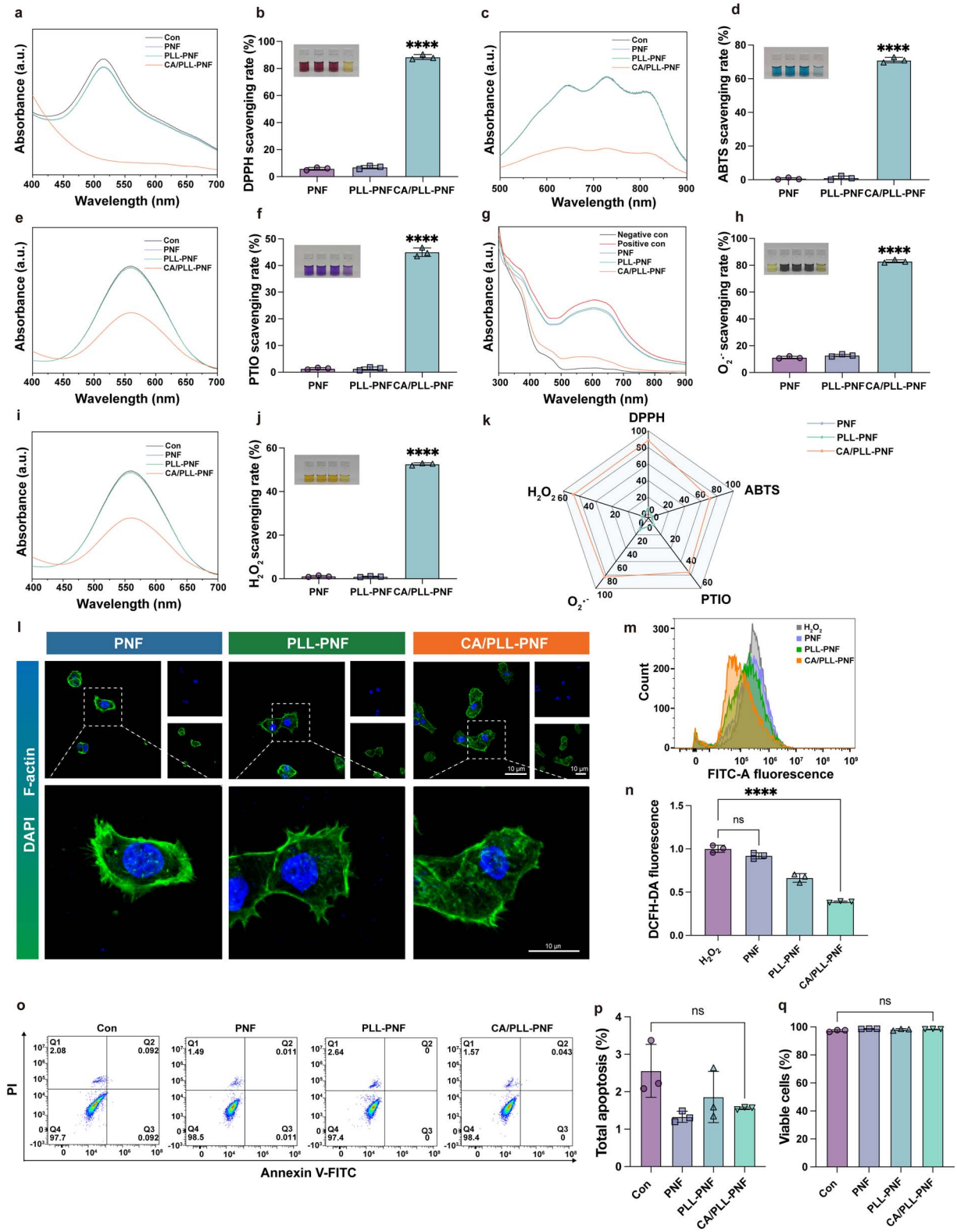


Figure 4 Radical scavenging capacity and cytoprotective effects against oxidative stress of the CA/PLL-PNF nanofibrous membrane. (**a**–**f**) Chemical radical clearance: UV–Vis spectra and scavenging rate quantification for the DPPH (a, b), ABTS (c, d), and PTIO (e, f) assays (****$P < 0.0001$). (**g**–**j**) Physiological ROS clearance: UV–Vis spectra and scavenging rate quantification for superoxide anions (g, h) and H_2O_2 (i, j) (****$P < 0.0001$). (**k**) Radar chart summarizing the comprehensive antioxidant capacity. (**l**) F-actin (green)/DAPI (blue) staining of cells cultured on different membranes. Scale bar: 10 μm. (**m**–**n**) Flow cytometric histograms (m) and quantification (n) of intracellular ROS levels (DCFH-DA) under H_2O_2-induced oxidative stress conditions (****$P < 0.0001$). (**o**–**q**) Cytotoxicity evaluation of membrane extracts: representative Annexin V/PI flow cytometry plots (o), total apoptosis rates (p), and cell viability (q) (ns). Statistical significance was assessed by one-way ANOVA with the Bonferroni correction or by an independent-samples *t* test; ****$P < 0.0001$. The experimental scheme was generated using BioRender.com with a license. *DPPH* 2,2-diphenyl-1-picrylhydrazyl, *PI* propidium iodide

Downloaded from academic.oup.com/burnstrauma/article/doi/10.1093/burnst/tkag036/8687358 by guest on 12 October 2026

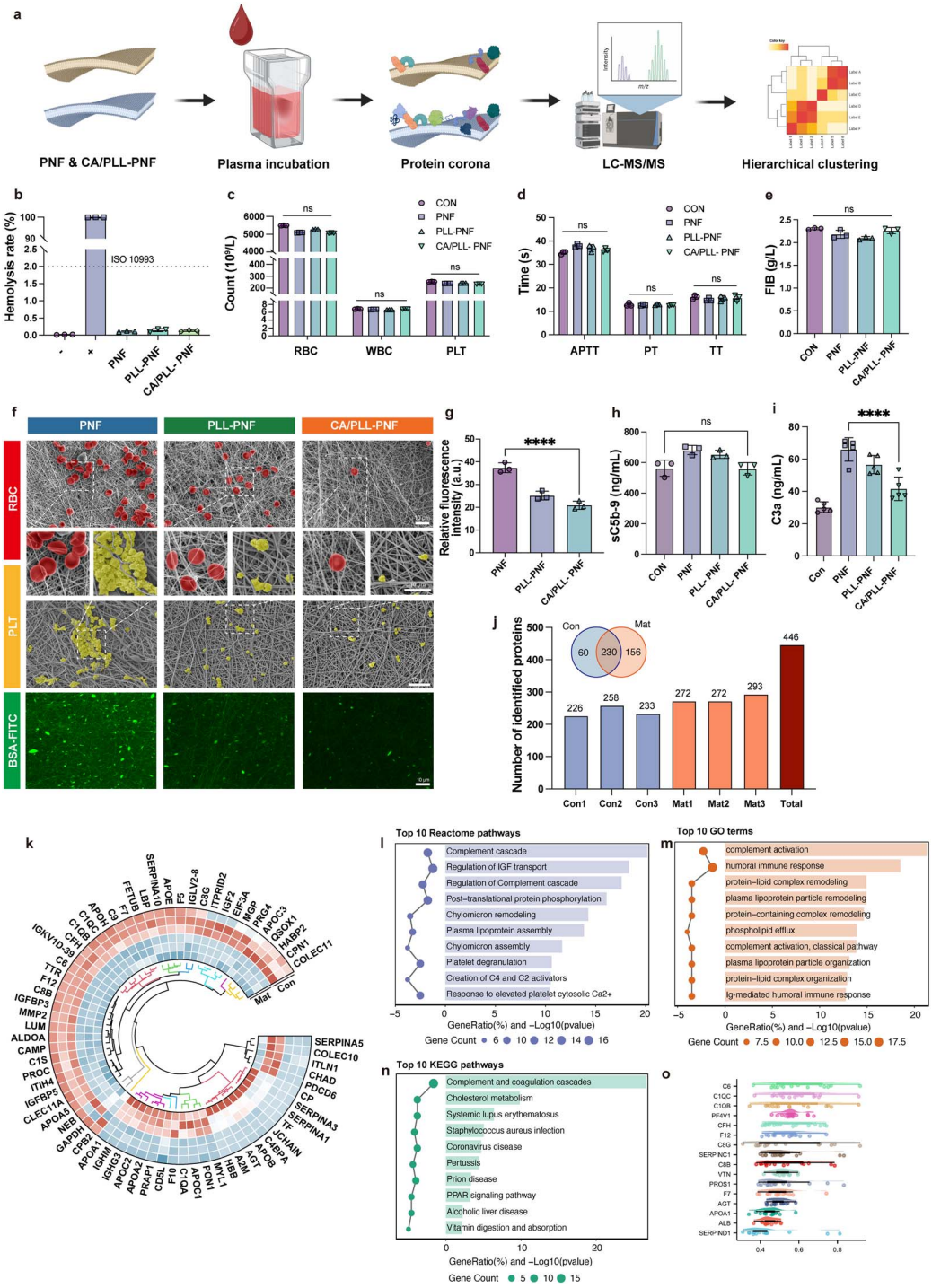


Figure 5 Hemocompatibility validation and plasma protein corona remodeling analysis of the CA/PLL-PNF interface. (**a**) Workflow for the protein corona proteomic analysis. The scheme was generated using BioRender.com with a license. (**b**) *In vitro* hemolysis rates evaluated against the ISO and ASTM thresholds. (**c**–**e**) Complete blood count indices (c), coagulation parameters (d), and FIB levels (e) following blood contact. (**f**–**g**) SEM images of erythrocyte and PLT adhesion (f) and fluorescence quantification of nonspecific BSA-FITC adsorption (g) (****$P < .0.0001$). Scale bar: 10 μm. (**h**–**i**) ELISA quantification of complement activation fragments C3a (h) (****$P < 0.0001$) and sC5b-9 (i) (ns). (**j**) Venn diagram and total count of proteins identified in the corona of the con (PNF) and mat (CA/PLL-PNF) groups. (**k**) Circular hierarchical clustering heatmap of differentially abundant proteins. (**l**–**n**) Enrichment analysis of differentially adsorbed proteins: Reactome Top10 (l), GO biological processes Top10 (m), and KEGG Top10 (n). (**o**) Scatter plot of differential protein abundances, highlighting the systematic downregulation of key complement recognition molecules and coagulation factors in the CA/PLL-PNF corona. Statistical significance was assessed by one-way ANOVA with Bonferroni correction; ****$P < 0.0001$. *PLL-PNF* poly-L-lysine-modified PNF, *ISO* International Organization for Standardization, *ASTM* American Society for Testing and Materials, *WBC* white blood cell, *PT* prothrombin time, *APTT* activated partial thromboplastin time, *TT*thrombin time, *BSA-FITC* fluorescein isothiocyanate–conjugated bovine serum albumin, *con* control (PNF), *mat* modified material (CA/PLL-PNF), *GO* Gene Ontology.

Downloaded from academic.oup.com/burnstrauma/article/doi/10.1093/burnst/tkag036/8687358 by guest on 12 October 2026

Table 1 Changes in renal function parameters after bilateral nephrectomy in Bama miniature pigs

Parameter	0 h	12 h	24 h	*P* value
CREA (μmol/L)	53.67 ± 6.51	276.33 ± 35.24*	521.00 ± 68.17**##	<0.01
UREA (mmol/L)	2.97 ± 0.25	10.84 ± 0.96*	17.90 ± 1.15**##	<0.01

Note: Data are presented as the mean ± SD. *$P < 0.05$, **$P < 0.01$ *vs* 0 h; #$P < 0.05$, ##$P < 0.01$ *vs* 12 h

Table 2 Changes in blood gas analysis and electrolyte parameters during RAD

Parameter	Group	0 h	1 h	2 h	3 h	4 h
pH	RAD	7.128 ± 0.024	7.178 ± 0.021	7.129 ± 0.028	7.134 ± 0.025	7.075 ± 0.030
	No-RAD	7.126 ± 0.023	7.142 ± 0.026	7.101 ± 0.031	7.062 ± 0.034	7.018 ± 0.038
PCO_2 (mmHg)	RAD	81.0 ± 4.9	87.6 ± 5.2	89.6 ± 5.8	85.6 ± 5.1	88.6 ± 5.6
	No-RAD	80.8 ± 5.1	88.9 ± 5.6	92.8 ± 6.0	94.6 ± 6.3	96.4 ± 6.8
HCO_3^- (mmol/L)	RAD	26.8 ± 1.6	32.5 ± 1.8	29.7 ± 1.5	28.7 ± 1.4	26.0 ± 1.5
	No-RAD	26.7 ± 1.7	30.1 ± 1.9	27.9 ± 1.8	25.8 ± 1.7	23.6 ± 1.9
BEecf (mmol/L)	RAD	−2.0 ± 0.8	4.0 ± 1.0	1.0 ± 0.8	0.0 ± 0.6	−4.0 ± 0.9
	No-RAD	−2.1 ± 0.9	2.0 ± 0.9	−1.0 ± 0.8	−3.0 ± 0.9	−5.0 ± 1.0
Na^+ (mmol/L)	RAD	133.0 ± 1.5	135.0 ± 1.4	133.0 ± 1.2	134.0 ± 1.3	133.0 ± 1.4
	No-RAD	133.0 ± 1.6	134.0 ± 1.5	133.0 ± 1.4	132.0 ± 1.6	132.0 ± 1.7
K^+ (mmol/L)	RAD	7.4 ± 0.3	6.8 ± 0.2	6.8 ± 0.3	7.1 ± 0.3	6.5 ± 0.2
	No-RAD	7.4 ± 0.3	7.2 ± 0.3	7.2 ± 0.5	7.1 ± 0.4	7.0 ± 0.4

Note: Data are presented as the mean ± SD. *PCO_2* partial pressure of carbon dioxide, *HCO_3^-* bicarbonate, *BEecf* base excess in extracellular fluid, *Na^+* sodium ion, *K^+* potassium ion

in the ISO 10993-4 standard. All complete blood count indices (RBC, Hb, HCT, MCV, MCH, MCHC, RDW) remained stable before and after material contact (Table S10). These results confirm that the bioreactor material poses no significant hemolytic risk or hematological toxicity and thus the material satisfies the safety prerequisites for large-animal extracorporeal circulation.

Preclinical validation of the bioartificial kidney device in a Bama miniature pig model of severe renal failure induced by bilateral nephrectomy

Establishment of severe renal failure induced by bilateral nephrectomy

To validate the RAD in a large-animal model, we established severe renal failure induced by bilateral nephrectomy in Bama miniature pigs. The surgical procedures were successfully completed in all 6 animals. Twelve hours after the surgeries, the serum creatinine (CREA) concentration increased from 53.67 ± 6.51 to 276.33 ± 35.24 μmol/L ($P < 0.05$), and the urea concentration increased from 2.97 ± 0.25 to 10.84 ± 0.96 mmol/L ($P < 0.05$), confirming the successful establishment of the model (Table 1).

Stable operation of the renal tubule assist device system for 4 hours without disruption of internal homeostasis

A standard clinical hemodialysis session typically lasts 4 h; thus, this duration served as the baseline target for device operation. The 4-h extracorporeal circulation was successfully completed in both the RAD and No-RAD groups. The primary circuit and the plasma separation-RAD branch remained patent throughout, and no continuous pressure abnormalities or severe coagulation events were observed. The dynamic changes in blood gas and electrolyte parameters during treatment are detailed in Table 2. Both groups exhibited a gradual decline in pH (RAD group: 7.128 → 7.075; No-RAD group: 7.126 → 7.018), which is consistent with the accumulation of acidic metabolites in an anephric state. The trends for PCO_2, HCO_3^-, and BEecf were similar between the two groups, while Na^+ and K^+ remained relatively stable throughout the treatment. These findings indicate that the integration of the RAD did not introduce additional disruptions to the internal homeostasis of the extracorporeal system.

Organ damage markers and inflammatory indices remain stable

To assess whether the RAD induced organ damage during extracorporeal circulation, we dynamically monitored markers of hepatic function (ALT and AST), myocardial injury (CK, CK-MB, and LDH), and systemic inflammation (CRP). ALT (Fig. 6b) and AST (Fig. 6c) levels exhibited minor fluctuations without progressive elevation. CK (Fig. 6d) and LDH (Fig. 6f) levels did not decrease. Although the level of CK-MB (Fig. 6e) was slightly elevated, the trend was similar in both groups, which was likely attributable to surgical anesthesia rather than to device toxicity. CRP levels (Fig. 6g) did not progressively increase. These results indicate that treatment with the RAD did not induce discernible organ damage during the 4-h observation period.

Evaluation of the renal replacement efficacy of the renal tubule assist device

Following the confirmation of device safety, we evaluated the renal replacement efficacy of the RAD. With respect to small-molecule toxins, both the CREA concentration and the urea

Downloaded from academic.oup.com/burnstrauma/article/doi/10.1093/burnst/tkag036/8687358 by guest on 12 October 2026

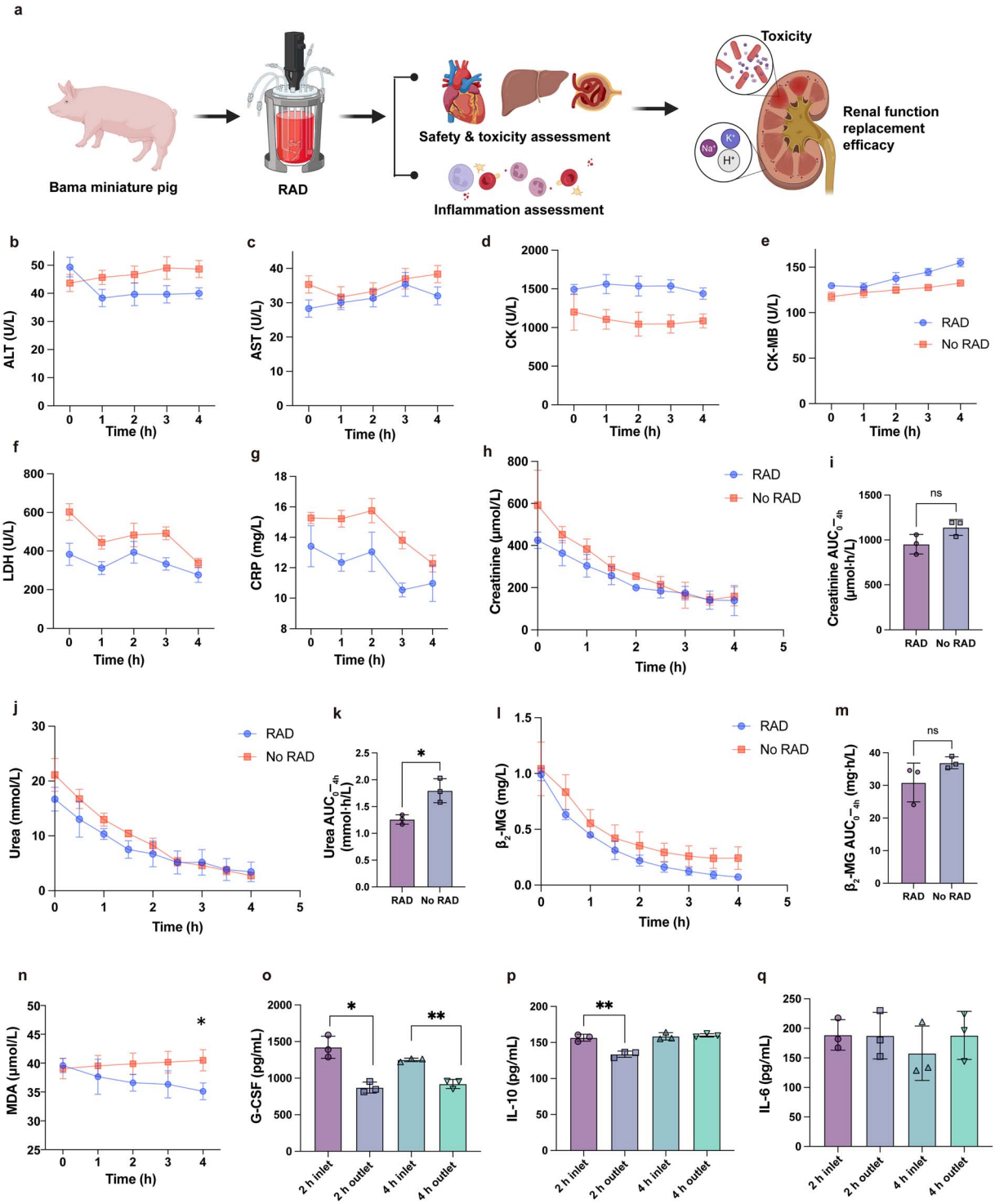


Figure 6 Safety, renal replacement efficacy, and biological support function of the RAD in a Bama miniature pig model of bilateral nephrectomy-induced severe renal failure. (**a**) Preclinical experimental workflow. A scheme was generated using BioRender.com with a license. (**b**–**g**) Dynamic monitoring of hepatic and myocardial injury markers and systemic inflammation: ALT (b), AST (c), CK (d), CK-MB (e), LDH (f), and CRP (g). (**h**–**k**) Small-molecule toxin clearance kinetics: CREA concentration curves (h) and the AUC (i); urea concentration curves (j) and the AUC (k) (ns). (**l**–**m**) Middle-molecule toxin clearance kinetics: β_2-MG concentration curves (l) and the AUC comparison (m) ($^*P < 0.05$). (n) Dynamic changes in circulating MDA levels during extracorporeal circulation. (**o**–**q**) Modulation of local inflammatory cytokines: concentration gradients of G-CSF (o), IL-10 (p), and IL-6 (q) across the RAD inlet and outlet at 2 h and 4 h; for time-course data (b–n), two-way repeated-measures ANOVA was used; when a significant interaction was detected, post hoc comparisons were performed with Šidák's correction. For cytokine inlet–outlet comparisons (o–q), the independent-samples *t* test was used. AUC comparisons (i, k, m) were performed using the independent-samples *t* test; $^*P < 0.05$, $^{**}P < 0.01$. *ALT* alanine aminotransferase, *AST* aspartate aminotransferase, *CK* creatine kinase, *CK-MB* creatine kinase MB isoenzyme

Downloaded from academic.oup.com/burnstrauma/article/doi/10.1093/burnst/tkag036/8687358 by guest on 12 October 2026

concentration decreased continuously over time in both groups (Fig. 6h–k), confirming the effective clearance function of the primary hemofiltration circuit. With respect to middle-molecule toxins, β_2-MG exhibited a more pronounced decline in the RAD group (Fig. 6l), which resulted in a significantly lower AUC in the RAD group than in the No-RAD group (1.260 ± 0.088 *vs* 1.797 ± 0.225 mg·h/L, $P = 0.018$) (Fig. 6m). This finding indicates that the cellular component of the RAD provides an independent, biologically driven clearance mechanism for middle-molecule toxins that are challenging to remove via conventional filtration.

Serum cystatin C levels decreased over time in both groups, but the difference was not significant (Figure S7), which suggests that the RAD-mediated biological clearance advantage may be molecule specific.

Immunomodulatory and antioxidant effects of the renal tubule assist device

To evaluate the *in vivo* antioxidant performance of the CA/PLL-PNF interface, we measured the levels of circulating MDA, a well-established end-product of lipid peroxidation. Two-way repeated-measures ANOVA revealed a significant time × group interaction ($P < 0.0001$). Post hoc analysis revealed that the MDA levels in the RAD group were significantly lower than those in the No-RAD group at 4 h (adjusted $P = 0.014$), whereas no significant difference was observed between 0 and 3 h (Fig. 6n). These results indicate that RAD progressively attenuated extracorporeal circulation–induced lipid peroxidation throughout the treatment period, which is consistent with the sustained radical-scavenging capacity of CA demonstrated *in vitro*. Supplementary oxidative stress biomarkers (serum catalase and glutathione reductase) showed trends consistent with the MDA findings (Figure S8).

Beyond toxin clearance, we assessed the ability of the device to modulate the inflammatory microenvironment by measuring the concentration gradient of cytokines across the RAD inlet and outlet. The concentration of the proinflammatory cytokine G-CSF at the outlet was significantly lower than that at the inlet at 2 h ($P < 0.05$) and 4 h ($P < 0.01$) (Fig. 6o), with the effect intensifying over time. These findings suggest that the device exerts a sustained and stable clearance effect on this cytokine. IL-10 levels at the outlet were lower than those at the inlet at 2 h ($P < 0.01$), but this difference disappeared by 4 h (Fig. 6p), potentially because of receptor saturation or the attainment of dynamic equilibrium. IL-6 levels remained stable between the inlet and outlet across all time points (Fig. 6q), which indicates that the RAD did not trigger additional proinflammatory cytokine release.

Discussion

This study establishes a comprehensive preclinical pipeline—from the establishment of functional seed cells and the construction of an antioxidant material interface to modular bioreactor fabrication and large-animal validation—and provides systematic experimental evidence for BAK-based organ support strategies in trauma and severe AKI.

Previous RAD/BAK studies have demonstrated that the integration of viable PT cells into extracorporeal circuits yields functional outputs beyond simple filtration. In animal models, RADs exhibit metabolic activities, such as glutathione degradation, ammoniagenesis, and 1,25-$(OH)_2$-D_3 synthesis [32], while also improving cardiovascular function and modulating systemic cytokines [33, 34]. This trend was echoed in early clinical trials, in which RAD treatment altered G-CSF, IL-6, and IL-10 levels [35], and thus this treatment demonstrated the potential to reduce 28-day mortality in a phase II randomized controlled trial [36]. Although subsequent phase IIb trials did not meet their primary endpoints, which has shifted the focus toward alternative strategies such as selective cytopheretic devices (SCDs) [37–39], the legacy of RAD research suggests that the supplementary biological effects mediated by cellular components remain crucial for improving severe AKI outcomes.

However, the transition from earlier BAK prototypes to stable, reproducible, and clinically applicable devices requires overcoming several critical bottlenecks: (i) a seed cell source that combines stable expansion capacity with the preservation of PT functional phenotypes; (ii) a cell-supporting substrate that not only facilitates adhesion but also minimizes protein adsorption, complement activation, and coagulation upon blood contact; and (iii) a bioreactor system that balances structural tunability, operational stability, and maneuverability in preclinical models. This study systematically addressed these three challenges through cellular engineering, interface modulation, and device fabrication.

Among these bottlenecks, securing a functional seed cell source is paramount. BAKs impose dual demands on seed cells: they must be capable of large-scale expansion to meet the required cell mass for device construction [10, 35] while strictly preserving the key functional phenotypes of the PT. These criteria are rarely met simultaneously by existing cell resources. HK-2 cells, immortalized via HPV 16 *E6/E7* [12], possess infinite proliferative capacity but exhibit impaired differentiation pathways because of E6-mediated p53 degradation and E7-mediated pRb antagonism [13, 14]. The ciPTEC line, which is generated via a temperature-sensitiveSV40 *Large T* and *hTERT* dual-gene strategy, proliferates at 33°C and differentiates at 37°C [15, 16]; however, this imposes operational complexity, and the functional recovery window during temperature shifts requires stringent control. We therefore opted for a conventional SV40 *Large T* single-gene immortalization strategy. Mechanistically, Large T abrogates cell cycle arrest by binding to p53 and pRb family proteins [17] but avoids the direct degradation of p53 that occurs with HPV E6, thereby causing less interference with differentiation phenotypes. iRTECs significantly outperformed HK-2 cells across the four functional dimensions of brush border enzyme activity, nitrogen metabolism, transmembrane water transport, and endocrine signal responsiveness, which indicates that SV40 *Large T* immortalization does not significantly compromise the core functional hallmarks of the PT.

After the functional phenotype of iRTECs was confirmed, we addressed the engineering challenge of scalable and reproducible cell supply by transitioning from 2D planar to 3D expansion, which was exemplified by a microcarrier-based spinner-flask system. An intermittent stirring strategy during the initial phase provided a window for cell–microcarrier collisions while preventing aggregation, thereby optimizing early attachment efficiency. Following expansion, the expression of CD13 and CD10 remained stable, while that of Ki67 increased, which demonstrates that the 3D dynamic environment effectively promoted proliferative activity but did not induce phenotypic drift. Furthermore, our preliminary exploration of the cryopreservation of intact microcarrier–cell complexes revealed that thawed units bypassed the reattachment step and directly entered spinner-flask expansion, thereby shortening the cell preparation cycle. While the BRECS

Downloaded from academic.oup.com/burnstrauma/article/doi/10.1093/burnst/tkag036/8687358 by guest on 12 October 2026

system developed by Humes' group adopted a more radical approach, which involved the cryopreservation of the entire cell-loaded bioreactor for direct clinical use [40], our microcarrier cryopreservation strategy, although it still requires a postthaw expansion phase, offers superior flexibility to adjust the expansion scale and device configuration according to specific clinical needs.

Beyond cells, the next critical element is the provision of an appropriate *in vitro* supporting interface. Traditional BAK materials act solely as passive adhesion substrates and immunoisolation barriers [10, 18] and lack intrinsic bioactivity. However, blood/plasma-material contact inevitably triggers protein adsorption, complement activation, and coagulation cascades—universal safety hazards for extracorporeal devices [20]. We engineered a CA/PLL-PNF-functionalized nanofibrous membrane utilizing CA to confer antioxidant activity while employing LbL assembly to alter surface chemistry and enhance hemocompatibility. The *ortho*-diphenol hydroxyl structure of CA scavenges free radicals via a hydrogen-donation mechanism, which generates relatively stable semiquinone radicals that form the chemical basis for its robust radical-scavenging ability [41, 42]. H_2O_2, the primary nonradical ROS *in vivo*, is markedly elevated in the pathological microenvironment of patients with trauma and severe AKI [19]. In the H_2O_2-induced oxidative stress model, CA/PLL-PNF significantly reduced intracellular ROS levels, which confirms that surface-anchored CA remains active at the cellular microenvironmental scale, and demonstrates the effective translation of chemical antioxidant capacity into active cytoprotection.

Concurrently, our protein corona proteomic data reveal a molecular mechanism—from protein adsorption to functional effects—for the superior hemocompatibility of CA/PLL-PNF. The competitive adsorption of plasma proteins onto material surfaces (the Vroman effect) results in the formation of a protein corona, which initiates the host immune response. The composition of the corona then dictates which immune-recognition ligands are exposed at the material–plasma interface [20, 21, 43, 44]. We found that complement recognition and attack molecules (e.g. C1Q, C6, C8) and coagulation factors (e.g. F7, F12) were systematically downregulated in the CA/PLL-PNF corona, which was accompanied by a significant reduction in C3a, whereas the level of sC5b-9 remained unchanged. While previous protein corona research has predominantly focused on the *in vivo* fate of nanoparticles [44], extending this concept to modulate the membrane–plasma interface in extracorporeal devices offers a novel paradigm for understanding and engineering hemocompatibility [45].

To further validate whether the surface-modulation properties of CA/PLL-PNF are preserved under pathological plasma conditions, we extended the protein corona analysis to plasma from patients with AKI and those with CKD (Figure S9). The results revealed disease-dependent shifts in corona composition: AKI plasma yielded coronas enriched in the humoral immune response and activation of the classical complement pathway, which reflects the elevated immunoglobulins and inflammatory mediators characteristic of AKI; in contrast, CKD plasma coronas were more prominently enriched in coagulation-related pathways (blood coagulation, hemostasis, PLT degranulation, fibrin clot formation), which is consistent with the widespread coagulation abnormalities observed in CKD. In contrast, the healthy plasma corona was dominated by lipoprotein particle remodeling and cholesterol metabolism pathways. Importantly, despite these compositional shifts, the complement and coagulation cascade pathways ranked consistently at the top of KEGG enrichment pathways across all three plasma conditions, and the differential protein adsorption direction of CA/PLL-PNF relative to the unmodified PNF control was maintained. This finding indicates that the functionalized interface retained its surface-modulation characteristics even in the context of disease-altered plasma protein profiles.

Notably, this antioxidant capacity was further corroborated *in vivo*: circulating MDA levels in the RAD group were significantly lower than those in the No-RAD group at 4 h (adjusted $P = 0.014$), which is consistent with observations from vitamin E-coated dialysis membranes and indicates that surface-anchored antioxidant activity can translate into measurable cytoprotection during extracorporeal circulation [46].

At the bioreactor level, traditional hollow-fiber filters are commercial products with rigid structural parameters that are difficult to adjust during the R&D phase [10, 25]. Our custom-designed, CNC-machined flat-plate bioreactor provides a cost-effective pathway for iterative development [27]. Its modular design allows individual disc layers to be extracted for testing without the need to dismantle the entire device, which is a capability that is lacking in closed hollow-fiber modules [26]. The absence of toxic leachables provided a material safety baseline for subsequent *in vivo* studies. At the large-animal systems level, the bilateral nephrectomy model offers a clear pathological background and high reproducibility and completely eliminates the confounding effects of residual renal function [47]. The RAD system demonstrated excellent engineering feasibility and biosafety during the 4-h operational window. The circuit remained patent without severe coagulation events. While circuit clotting previously limited operational time in early large-animal studies performed by the Humes group [10, 35], the plasma separation step introduced in our study, although it increased system complexity, did not compromise circuit stability. Blood gas analysis revealed a gradual decrease in pH across both groups, which was consistent with the accumulation of acidic metabolites in the anephric state; importantly, the RAD did not exacerbate this trend. The levels of electrolytes remained stable, indicating that no additional disruption to internal homeostasis occurred. Biomarkers of organ damage (ALT and AST) did not progressively increase. The slight increase in CK-MB, which was consistent across both groups, was likely related to general anesthesia and surgical stress rather than to device-specific toxicity, which aligns with the short-term safety profiles reported by Humes *et al.* in canine and porcine models [33, 35]. The absence of progressive CRP elevation further supports the device's systemic biosafety.

With respect to xenogeneic immunocompatibility, the enclosed extracorporeal design, in which only cell-free plasma contacts iRTECs and a secondary plasma separator prevents cell escape, limits direct cell–host tissue interaction. No overt acute adverse events were observed during the 4-h operation, which is consistent with reports from the Humes group and Johnston *et al.* in which human renal cells in porcine extracorporeal circuits were used [35, 48, 49].

The statistically significant difference in the β_2-MG AUC between the two groups ($P = 0.018$) is the most compelling functional finding of this study. β_2-MG (molecular weight $\sim$ 11.8 kDa) is a middle-molecule toxin with poor convective clearance by conventional dialysis membranes [50, 51]. Consequently, this protein serves as an effective surrogate to detect the biological

Downloaded from academic.oup.com/burnstrauma/article/doi/10.1093/burnst/tkag036/8687358 by guest on 12 October 2026

clearance mediated by the RAD cellular unit. Saito *et al.* reported similar preferential middle-molecule clearance across different BAK configurations [52, 53].

Furthermore, G-CSF levels across the bioreactor decreased significantly at 2 h and 4 h, and the effect intensified over time, which demonstrates consistent active regulation. In trauma and severe AKI, G-CSF stimulates the bone marrow to release neutrophils, whose subsequent infiltration exacerbates inflammatory damage to the kidney and distant organs [54]. In their phase I/II clinical trials, the Humes group reported that reductions in G-CSF after RAD treatment were positively correlated with improved 28-day survival [35, 36]. Potential mechanisms include receptor-mediated endocytic degradation by PT cells and nonspecific adsorption by the high-surface-area nanofibrous interface [54], although their relative contributions require further elucidation. The directional change in IL-10 at 2 h, which disappeared by 4 h, may reflect receptor saturation or the attainment of dynamic equilibrium. The stability of IL-6 across all time points reinforces the safety profile and indicates that the RAD does not induce extraneous proinflammatory cytokine release.

This study has several limitations. First, the observation period was limited to 4 h, which approximates a single clinical dialysis session but is insufficient to evaluate longer-term device safety, sustained cellular function, or the longer-term *in vivo* antioxidant efficacy of the CA/PLL-PNF interface. Moreover, only heparin-based anticoagulation was employed; the device's performance under alternative strategies, such as regional citrate anticoagulation and in the setting of coagulopathy, which are frequently encountered in critically ill AKI patients, remains to be evaluated. Second, although the bilateral nephrectomy model effectively eliminated the confounding effect of residual renal function, this model recapitulates absolute anephria rather than the more complex pathophysiology of clinical AKI, which includes ischemia–reperfusion or sepsis-associated injury. Thus, the current findings should be interpreted primarily as short-term proof-of-concept and system-integration validation. Third, the biosafety of iRTECs requires further investigation. SV40 *Large T*-immortalized human cells were used in a porcine extracorporeal system, and no acute adverse events were observed during the 4-h run. Although a secondary plasma separator was incorporated downstream of the RAD as a cell-retention filter to prevent potential cell escape into the host circulation, additional studies are needed to systematically assess genomic stability, tumorigenic potential, and xenogeneic immunocompatibility. Fourth, the current functional evaluation remains incomplete. Toxin clearance was assessed using representative middle-molecules only, without the inclusion of larger uremic solutes or protein-bound toxins. In addition, although the exploratory protein corona results obtained with AKI and CKD patient-derived plasma suggested preserved surface-modulating properties of CA/PLL-PNF across disease backgrounds, these findings still require validation in larger and better stratified cohorts.

Conclusions

In this study, an RAD platform encompassing seed cell preparation, antioxidant material interface construction, device integration, and large-animal validation was established. The iRTEC cell line exhibits both key PT functions and a robust scalable expansion capacity. The LbL self-assembly of CA/PLL endows the nanofibrous membrane with bioactive functions, including antioxidant protection and protein corona modulation, thereby transitioning the material interface from a passive carrier to a functionalized substrate. Furthermore, the CNC-machined multilayer flat-plate bioreactor provides a highly tunable engineering platform for rapid and cost-effective iteration. In the Bama miniature pig model of bilateral nephrectomy, the system maintained stable extracorporeal circulation for 4 h. The integration of the viable cell unit facilitated the supplementary clearance of middle-molecule toxins (as evidenced by a significantly reduced β_2-MG AUC, $P = 0.018$) and modulated the local inflammatory microenvironment (as indicated by a sustained reduction in G-CSF, $P < 0.05$), whereas the antioxidant interface attenuated extracorporeal circulation-induced lipid peroxidation *in vivo* (as reflected by the significantly lower circulating MDA concentration at 4 h, $P = 0.014$). These findings provide multidimensional preclinical evidence—from the cellular and material levels to the systemic level—for advanced organ support strategies in trauma- and critical illness-associated AKI.

Acknowledgements

The authors would like to express their sincere gratitude to Professor Yuanda Wang from the Department of Nephrology, First Medical Center, Chinese PLA General Hospital, for his valuable support and assistance during this study. The authors also thank Zeyang Yu from the outpatient blood purification unit for assistance with the related work.

Author contributions

Yunming Xiao (Data curation [equal], Formal analysis [equal], Investigation [equal], Validation [equal], Visualization [equal], Writing—original draft [equal], Writing—review & editing [equal]), Chuyue Zhang (Data curation [equal], Formal analysis [equal], Investigation [equal], Validation [equal], Visualization [equal], Writing—original draft [equal], Writing—review & editing [equal]), Tianyi Yang (Software [equal], Validation [equal], Visualization [equal], Writing—original draft [equal], Writing—review & editing [equal]), Yiyu Huang (Data curation [supporting], Formal analysis [supporting], Investigation [supporting], Validation [supporting]), Xu Wang (Data curation [supporting], Formal analysis [supporting], Investigation [supporting], Validation [supporting]), Xiaoxiao Liu (Data curation [supporting], Formal analysis [supporting], Investigation [supporting], Validation [supporting]), Mengfei Li (Data curation [supporting], Formal analysis [supporting], Investigation [supporting], Validation [supporting]), Shaoyuan Cui (Data curation [supporting], Formal analysis [supporting], Investigation [supporting], Validation [supporting]), Guangrui Geng (Data curation [supporting], Formal analysis [supporting], Investigation [supporting], Validation [supporting]), Xiang Li (Conceptualization [equal], Methodology [equal], Resources [equal], Supervision [equal], Writing—original draft [supporting]), Qinggang Li (Conceptualization [equal], Funding acquisition [lead], Methodology [equal], Resources [equal], Supervision [equal], Writing—review & editing [supporting]), Xiangmei Chen (Conceptualization [equal], Funding acquisition [lead], Methodology [equal], Project administration [lead], Resources [equal], Supervision [equal], Writing—original draft [equal], Writing—review & editing [equal]).

Downloaded from academic.oup.com/burnstrauma/article/doi/10.1093/burnst/tkag036/8687358 by guest on 12 October 2026

Supplementary material

Supplementary material is available at *Burns & Trauma* online.

Ethics approval and consent to participate

Human kidney tissues were obtained from the normal cortex at the tumor-distant pole of kidneys resected from patients undergoing total nephrectomy, and plasma for the protein corona experiments was collected from healthy volunteers as well as from patients with AKI and CKD. Informed consent was obtained for all sample collections. Both the human studies and the Bama miniature pig experiments were approved bythe Ethics Committee of the Chinese PLA General Hospital (Approval No. S2022-640-01) and conducted in strict accordance with relevant ethical guidelines.

Conflicts of interest

The authors declare that they have no conflict of interest.

Funding

This work was supported by the Sichuan Science and Technology Program [grant numbers 2025ZNSFSC1602, 2022YFS0328]; and the National Natural Science Foundation of China [grant number 82200764].

Data availability

The mass spectrometry proteomics data generated in this study have been deposited in the iProX repository under subproject ID IPX0015336001 and are publicly available.

References

1. Hoste EA, Bagshaw SM, Bellomo R, Cely CM, Colman R, Cruz DN, *et al.* Epidemiology of acute kidney injury in critically ill patients: the multinational AKI-EPI study. *Intensive Care Med* 2015;41:1411–23. https://doi.org/10.1007/s00134-015-3934-7.
2. Mosier MJ, Pham TN, Klein MB, Gibran NS, Arnoldo BD, Gamelli RL, *et al.* Early acute kidney injury predicts progressive renal dysfunction and higher mortality in severely burned adults. *J Burn Care Res* 2010;31:83–92. https://doi.org/10.1097/BCR.0b013e3181cb8c87.
3. Clark A, Neyra JA, Madni T, Imran J, Phelan H, Arnoldo B, *et al.* Acute kidney injury after burn. *Burns* 2017;43:898–908. https://doi.org/10.1016/j.burns.2017.01.023.
4. Kellum JA, Romagnani P, Ashuntantang G, Ronco C, Zarbock A, Anders HJ Acute kidney injury. *Nat Rev Dis Primers* 2021;7:52. https://doi.org/10.1038/s41572-021-00284-z.
5. Uchino S, Kellum JA, Bellomo R, Doig GS, Morimatsu H, Morgera S, *et al.* Acute renal failure in critically ill patients: a multinational, multicenter study. *Jama* 2005;294:813–8. https://doi.org/10.1001/jama.294.7.813.
6. Ronco C, Bellomo R, Kellum JA. Acute kidney injury. *Lancet* 2019;394:1949–64. https://doi.org/10.1016/S0140-6736(19)32563-2.
7. Humes HD. Bioartificial kidney for full renal replacement therapy [J]. *Semin Nephrol* 2000;20:71–82.
8. Curthoys NP, Moe OW. Proximal tubule function and response to acidosis. *Clin J Am Soc Nephrol* 2014;9:1627–38. https://doi.org/10.2215/CJN.10391012.
9. Zhuo JL, Li XC. Proximal nephron. *Compr Physiol* 2013;3:1079–123. https://doi.org/10.1002/j.2040-4603.2013.tb00514.x.
10. Humes HD, Mackay SM, Funke AJ, Buffington DA The bioartificial renal tubule assist device to enhance CRRT in acute renal failure. *Am J Kidney Dis* 1997;30:S28–31. https://doi.org/10.1016/S0272-6386(97)90539-4.
11. Humes HD, Buffington DA, Mackay SM, Funke AJ, Weitzel WF Replacement of renal function in uremic animals with a tissue-engineered kidney. *Nat Biotechnol* 1999;17:451–5. https://doi.org/10.1038/8626.
12. Ryan MJ, Johnson G, Kirk J, Fuerstenberg SM, Zager RA, Torok-Storb B HK-2: an immortalized proximal tubule epithelial cell line from normal adult human kidney. *Kidney Int* 1994;45:48–57. https://doi.org/10.1038/ki.1994.6.
13. Jenkinson SE, Chung GW, Van Loon E, Bakar NS, Dalzell AM, Brown CDA The limitations of renal epithelial cell line HK-2 as a model of drug transporter expression and function in the proximal tubule. *Pflugers Arch* 2012;464:601–11. https://doi.org/10.1007/s00424-012-1163-2.
14. Aschauer L, Gruber LN, Pfaller W, Limonciel A, Athersuch TJ, Cavill R, *et al.* Delineation of the key aspects in the regulation of epithelial monolayer formation. *Mol Cell Biol* 2013;33:2535–50. https://doi.org/10.1128/MCB.01435-12.
15. Wilmer MJ, Saleem MA, Masereeuw R, Ni L, van der Velden TJ, Russel FG, *et al.* Novel conditionally immortalized human proximal tubule cell line expressing functional influx and efflux transporters. *Cell Tissue Res* 2010;339:449–57. https://doi.org/10.1007/s00441-009-0882-y.
16. Jansen J, Schophuizen CMS, Wilmer MJ, Lahham SHM, Mutsaers HAM, Wetzels JFM, *et al.* A morphological and functional comparison of proximal tubule cell lines established from human urine and kidney tissue. *Exp Cell Res* 2014;323:87–99. https://doi.org/10.1016/j.yexcr.2014.02.011.
17. Wieser M, Stadler G, Jennings P, Streubel B, Pfaller W, Ambros P, *et al.* hTERT alone immortalizes epithelial cells of renal proximal tubules without changing their functional characteristics. *Am J Physiol Renal Physiol* 2008;295:F1365–75. https://doi.org/10.1152/ajprenal.90405.2008.
18. Song JH, Humes HD. The bioartificial kidney in the treatment of acute kidney injury. *Curr Drug Targets* 2009;10:1227–34. https://doi.org/10.2174/138945009789753273.
19. Ratliff BB, Abdulmahdi W, Pawar R, Wolin MS Oxidant mechanisms in renal injury and disease. *Antioxid Redox Signal* 2016;25:119–46. https://doi.org/10.1089/ars.2016.6665.
20. Gorbet MB, Sefton MV. Biomaterial-associated thrombosis: roles of coagulation factors, complement, platelets and leukocytes. *Biomaterials* 2004;25:5681–703. https://doi.org/10.1016/j.biomaterials.2004.01.023.
21. Cedervall T, Lynch I, Lindman S, Berggård T, Thulin E, Nilsson H, *et al.* Understanding the nanoparticle-protein corona using methods to quantify exchange rates and affinities of proteins

Downloaded from academic.oup.com/burnstrauma/article/doi/10.1093/burnst/tkag036/8687358 by guest on 12 October 2026

for nanoparticles. *Proc Natl Acad Sci U S A* 2007;104:2050–5. https://doi.org/10.1073/pnas.0608582104.
22. Xue J, Wu T, Dai Y, Xia Y Electrospinning and electrospun nanofibers: methods, materials, and applications. *Chem Rev* 2019;119:5298–415. https://doi.org/10.1021/acs.chemrev.8b00593.
23. Bhardwaj N, Kundu SC. Electrospinning: a fascinating fiber fabrication technique. *Biotechnol Adv* 2010;28:325–47. https://doi.org/10.1016/j.biotechadv.2010.01.004.
24. Richardson JJ, Björnmalm M, Caruso F. Multilayer assembly. Technology-driven layer-by-layer assembly of nanofilms. *Science* 2015;348:aaa2491. https://doi.org/10.1126/science.aaa2491.
25. Jansen J, Fedecostante M, Wilmer MJ, Peters JG, Kreuser UM, van den Broek PH, *et al.* Bioengineered kidney tubules efficiently excrete uremic toxins. *Sci Rep* 2016;6:26715. https://doi.org/10.1038/srep26715.
26. Papenburg BJ, Vogelaar L, Bolhuis-Versteeg LA, Lammertink RGH, Stamatialis D, Wessling M One-step fabrication of porous micropatterned scaffolds to control cell behavior. *Biomaterials* 2007;28:1998–2009. https://doi.org/10.1016/j.biomaterials.2006.12.023.
27. Murphy SV, Atala A. 3D bioprinting of tissues and organs. *Nat Biotechnol* 2014;32:773–85. https://doi.org/10.1038/nbt.2958.
28. Tate SS, Meister A. Gamma-glutamyl transpeptidase: catalytic, structural and functional aspects. *Mol Cell Biochem* 1981;39:357–68. https://doi.org/10.1007/BF00232585.
29. Weiner D I, Verlander JW. Renal ammonia metabolism and transport. *Compr Physiol* 2013;3:201–20. https://doi.org/10.1002/j.2040-4603.2013.tb00491.x.
30. Nielsen S, Frøkiaer J, Marples D, Kwon TH, Agre P, Knepper MA Aquaporins in the kidney: from molecules to medicine. *Physiol Rev* 2002;82:205–44. https://doi.org/10.1152/physrev.00024.2001.
31. Jüppner H, Abou-Samra AB, Freeman M, Kong XF, Schipani E, Richards J, *et al.* A G protein-linked receptor for parathyroid hormone and parathyroid hormone-related peptide. *Science* 1991;254:1024–6. https://doi.org/10.1126/science.1658941.
32. Humes HD, Fissell WH, Weitzel WF, Buffington DA, Westover AJ, MacKay SM, *et al.* Metabolic replacement of kidney function in uremic animals with a bioartificial kidney containing human cells. *Am J Kidney Dis* 2002;39:1078–87. https://doi.org/10.1053/ajkd.2002.32792.
33. Fissell WH, Lou L, Abrishami S, Buffington DA, Humes HD Bioartificial kidney ameliorates gram-negative bacteria-induced septic shock in uremic animals. *J Am Soc Nephrol* 2003;14:454–61. https://doi.org/10.1097/01.ASN.0000045046.94575.96.
34. Humes HD, Buffington DA, Lou L, Abrishami S, Wang M, Xia J, *et al.* Cell therapy with a tissue-engineered kidney reduces the multiple-organ consequences of septic shock. *Crit Care Med* 2003;31:2421–8. https://doi.org/10.1097/01.CCM.0000089644.70597.C1.
35. Humes HD, Weitzel WF, Bartlett RH, Swaniker FC, Paganini EP, Luderer JR, *et al.* Initial clinical results of the bioartificial kidney containing human cells in ICU patients with acute renal failure. *Kidney Int* 2004;66:1578–88. https://doi.org/10.1111/j.1523-1755.2004.00923.x.
36. Tumlin J, Wali R, Williams W, Murray P, Tolwani AJ, Vinnikova AK, *et al.* Efficacy and safety of renal tubule cell therapy for acute renal failure. *J Am Soc Nephrol* 2008;19:1034–40. https://doi.org/10.1681/ASN.2007080895.
37. Johnston KA, Westover AJ, Rojas-Pena A, Buffington DA, Pino CJ, Smith PL, *et al.* Development of a wearable bioartificial kidney using the bioartificial renal epithelial cell system (BRECS). *J Tissue Eng Regen Med* 2017;11:3048–55. https://doi.org/10.1002/term.2206.
38. Ding F, Song JH, Jung JY, Lou L, Wang M, Charles L, *et al.* A biomimetic membrane device that modulates the excessive inflammatory response to sepsis. *PLoS One* 2011;6:e18584. https://doi.org/10.1371/journal.pone.0018584.
39. Tumlin JA, Chawla L, Tolwani AJ, Mehta R, Dillon J, Finkel KW, *et al.* The effect of the selective cytopheretic device on acute kidney injury outcomes in the intensive care unit: a multicenter pilot study. *Semin Dial* 2013;26:616–23. https://doi.org/10.1111/sdi.12032.
40. Buffington DA, Pino CJ, Chen L, Westover AJ, Hageman G, Humes HD Bioartificial renal epithelial cell system (BRECS): a compact, cryopreservable extracorporeal renal replacement device. *Cell Med* 2012;4:33–44. https://doi.org/10.3727/215517912X653328.
41. Naveed M, Hejazi V, Abbas M, Kamboh AA, Khan GJ, Shumzaid M, *et al.* Chlorogenic acid (CGA): a pharmacological review and call for further research. *Biomed Pharmacother* 2018;97:67–74. https://doi.org/10.1016/j.biopha.2017.10.064.
42. Liang N, Kitts DD. Role of chlorogenic acids in controlling oxidative and inflammatory stress conditions. *Nutrients* 2015;8:16. https://doi.org/10.3390/nu8010016.
43. Vroman L, Adams AL. Identification of rapid changes at plasma-solid interfaces. *J Biomed Mater Res* 1969;3:43–67. https://doi.org/10.1002/jbm.820030106.
44. Monopoli MP, Aberg C, Salvati A, Dawson KA Biomolecular coronas provide the biological identity of nanosized materials. *Nat Nanotechnol* 2012;7:779–86. https://doi.org/10.1038/nnano.2012.207.
45. Ekdahl KN, Lambris JD, Elwing H, Ricklin D, Nilsson PH, Teramura Y, *et al.* Innate immunity activation on biomaterial surfaces: a mechanistic model and coping strategies. *Adv Drug Deliv Rev* 2011;63:1042–50. https://doi.org/10.1016/j.addr.2011.06.012.
46. Sommerburg, Sostmann K, Grune T, Ehrich JH Oxidative stress in hemodialysis patients treated with a dialysis membrane which has alpha-tocopherol bonded to its surface. *Biofactors* 1999;10:121–4. https://doi.org/10.1002/biof.5520100206.
47. Yamamoto S, Umeno H, Sano Y, Koremoto M, Goda Y, Kaneko Y, *et al.* A chronic intermittent haemodialysis pig model for functional evaluation of dialysis membranes. *Int J Artif Organs* 2024;47:321–8. https://doi.org/10.1177/03913988241253152.
48. Humes HD, Fissell WH, Weitzel WF. The bioartificial kidney in the treatment of acute renal failure. *Kidney Int Suppl* 2002;61:S121–5. https://doi.org/10.1046/j.1523-1755.61.s80.22.x.
49. Westover AJ, Buffington DA, Johnston KA, Smith PL, Pino CJ, Humes HD A bio-artificial renal epithelial cell system conveys survival advantage in a porcine model of septic shock. *J Tissue Eng Regen Med* 2017;11:649–57. https://doi.org/10.1002/term.1961.

Downloaded from academic.oup.com/burnstrauma/article/doi/10.1093/burnst/tkag036/8687358 by guest on 12 October 2026

50. Cheung AK, Rocco MV, Yan G, Leypoldt JK, Levin NW, Greene T, *et al.* Serum beta-2 microglobulin levels predict mortality in dialysis patients: results of the HEMO study. *J Am Soc Nephrol* 2006;17:546–55. https://doi.org/10.1681/ASN.2005020132.
51. Locatelli F, Martin-Malo A, Hannedouche T, Loureiro A, Papadimitriou M, Wizemann V, *et al.* Effect of membrane permeability on survival of hemodialysis patients. *J Am Soc Nephrol* 2009;20:645–54. https://doi.org/10.1681/ASN.2008060590.
52. Saito A, Aung T, Sekiguchi K, Sato Y Present status and perspective of the development of a bioartificial kidney for chronic renal failure patients. *Ther Apher Dial* 2006;10:342–7. https://doi.org/10.1111/j.1744-9987.2006.00387.x.
53. Saito A, Sawada K, Fujimura S, Suzuki H, Hirukawa T, Tatsumi R, *et al.* Evaluation of bioartificial renal tubule device prepared with lifespan-extended human renal proximal tubular epithelial cells. *Nephrol Dial Transplant* 2012;27:3091–9. https://doi.org/10.1093/ndt/gfr755.
54. Bussolati B, David S, Cambi V, Tobias P, Camussi G Urinary soluble CD14 mediates human proximal tubular epithelial cell injury induced by LPS. *Int J Mol Med* 2002;10:441–9. https://doi.org/10.3892/ijmm.10.4.441.

Downloaded from academic.oup.com/burnstrauma/article/doi/10.1093/burnst/tkag036/8687358 by guest on 12 October 2026

© The Author(s) 2026. Published by Oxford University Press. This is an Open Access article distributed under the terms of the Creative Commons Attribution-NonCommercial License (https://creativecommons.org/licenses/by-nc/4.0/), which permits non-commercial re-use, distribution, and reproduction in any medium, provided the original work is properly cited. For commercial re-use, please contact reprints@oup.com for reprints and translation rights for reprints. All other permissions can be obtained through our RightsLink service via the Permissions link on the article page on our site—for further information please contact journals.permissions@oup.com.
Burns & Trauma, 2026, 14, tkag036
https://doi.org/10.1093/burnst/tkag036
Research Article